,

A level set projection model of lipid vesicles in general flows[☆]

D. Salac[a], M. Miksis[a]

[a]*Northwestern University, Engineering Sciences and Applied Mathematics, Evanston, IL, 60208*

Abstract

A new numerical method to model the dynamic behavior of lipid vesicles under general flows is presented. A gradient-augmented level set method is used to model the membrane motion. To enforce the volume- and surface-incompressibility constraints a four-step projection method is developed to integrate the full Navier-Stokes equations. This scheme is implemented on an adaptive non-graded Cartesian grid. Convergence results are presented, along with sample two-dimensional results of vesicles under various flow conditions.

Keywords: Lipid vesicle, Projection method, Level set, Fluid membrane, Numerical method

1. Introduction

Lipid molecules introduced into aqueous solutions will self-assemble into fluid-filled vesicles to minimize free energy. These vesicles have been of recent interest as a model system for non-nucleated biological cells such as red-blood cells [1], showing similar equilibrium shapes [2] and non-equilibrium behavior such as tumbling [3, 4]. Vesicles have also been proposed as possible drug delivery systems [5], which would allow for targeted drug therapies, and as possible biological micro-reactors for extremely small scale reactions [6, 7]. To be of general use the behavior of lipid vesicles in general fluid flows must be understood. The response of vesicles to external flows is due to a competition between the bending, in-extension, and hydrodynamic forces acting on the vesicle membrane. This is non-trivial behavior and in most cases can not be determined *a priori*.

Recent experimental work with vesicles has demonstrated a rich and varied behavior in response to viscous fluid flow. A transition in behavior was observed to depend on the material properties of the system, specifically the viscosity ratio between the encapsulated and surrounding fluids [3, 4]. Vesicles in Poiseuille flow have been shown to migrate towards the centerline of the flow [8, 9], unlike solid particles which do not

demonstrate cross-stream migration [10]. Vesicles in wall-bounded shear flow have also been shown to experience a lifting force in response to the flow field [11].

To better understand the behavior of lipids vesicles theoretical and numerical investigations have appeared. A number of studies on nearly-spherical vesicles in linear flows have been performed, recovering behavior observed experimentally [12, 13]. Theoretical analysis also predicts behavior not yet observed experimentally, including lipid density variations in the membrane [14] and various modes of motion [15].

Numerical investigations of lipid vesicle motion have also been performed. Some of these do not include an external fluid and instead focus on the bending effects of the membrane [16, 17]. Most of the works that do include fluid effects investigate creeping flow, as characterized by Reynolds numbers much less than one. Included in the previous investigations are models based on the phase-field method [18, 19, 20, 21, 22, 23], boundary integral formulations [22, 24, 25, 26, 27], and spectral methods [28]. In the creeping flow regime these models match well with known experimental and analytical results and have been able to track multiple vesicles [25].

Many previous numerical investigations of lipid vesicles look at only the limitation of creeping flow. To use vesicles as a model for red blood cells and as a drug delivery system the behavior of vesicles in physiological situations must be addressed. Consider the human cardiovascular system. Creeping flow is observed in human capillaries [29]. If other areas are considered, though, this is no longer true. The shear rate in arterioles is on the order of 8000 s^{-1} while the diameter is approximitly 50 μm [30]. Consider a lipid vesicle with a diameter of 40 μm being used as a drug delivery mechanism. This gives a velocity difference across the vesicles of 0.32 m/s. Using a blood density of 1050 kg/m^3 [31] and a viscosity of 6×10^{-3}Pa s [30] this gives a Reynolds number of 2.24, well outside of the creeping flow regime. To allow for investigations of vesicles in a wide range of flow conditions a new model must be developed

In section 2 the problem formulation is presented, including the derivation of the interfacial membrane conditions. Section 3 details the numerical implementation of the model. Two-dimensional numerical results and verification are presented in Section 4. Future work, including extension to three dimensional simulations, is discussed in the conclusions.

2. Development of the Model

Consider a single vesicle suspended in a viscous flow. The fluid enclosed by the vesicle may have different material properties than the surrounding fluid. The response of the vesicle to the external flow will depend on the various forces acting on the vesicle membrane. These forces can be determined by examining the free energy of the closed membrane.

The total free energy of a vesicle membrane has contributions from the bending of the membrane, the total number of lipids in the membrane, and the total encapsulated volume [2]. The bending energy contribution is directly related to the bending rigidity of a lipid membrane. This bending rigidity has a magnitude comparable to the thermal energy, on the order of 10^{-19} J [32]. The total energy contribution from the total number of lipids in the membrane relates to the area compression modulus of a lipid membrane, which has a magnitude about 250 mN/m [32]. Considering a spherical

vesicle with a radius of 10 μm this leads to an energy contribution on the order of 10^{-10} J, much larger than the contribution from bending and the thermal energy. The energy associated with the encapsulated volume is due to the osmotic pressure induced by concentration variations between the inner and outer fluids. This energy scales as $RTcV/2$, where $R \approx 8.31$ $JmolK^{-1}$ is the gas constant, T is the temperature, c is the total concentration in moles per unit volume of the active molecules, and V is the enclosed volume [2]. Again taking a vesicle with a radius of 10 μm and assuming a concentration of $c = 10^{-4}$ mol m^{-3} this leads to an energy contribution on the order of 10^{-16} J, much larger than the bending contribution and the thermal energy [2]. For the systems of interest there is not enough energy in the system to change the number of lipids on the membrane or the enclosed volume. Thus these two quantities are considered fixed for a given vesicle. The high compressibility modulus of a lipid membrane indicates that the number of lipids directly relates to the local surface area of a vesicle. Thus the local surface area, in addition to the enclosed volume, is fixed. This information will influence the hydrodynamic equations in the next section. In Section 5.3 we will give an example illustrating the difference between solutions found enforcing only the global area constraint and solutions which satisfy the surface incompressibility constraint. See Ref. [2] for additional discussion of these constraints.

The local incompressibility of the vesicle interface makes this a challenging problem in comparison to the dynamics of drops and bubbles. Enforcing the surface incompressibility is the novel aspect of the numerical methods that have been designed to study this problem. A number of previous approaches assume that the membrane is a thin elastic shell. This approach has been used to study the dynamics of red blood cells and leukocytes [26, 27]. With the proper choice of parameters the surface area is almost conserved. For bilayer vesicles the model due to Helfrich [2, 33] has become the accepted model, showing good agreement between theory and experiment. This model accounts for the bending rigidity of the interface and enforces the surface incompressibility as an additional constraint. How to enforce this constraint in a computational method has been a topic of significant research. In the Stokes flow limit [25, 29, 34] this is usually done by allowing surface tension to be a Lagrange multiplier selected to enforce the local area constraint. Another approach recently proposed by Ghigliotti *et al.* [22] uses a penalty method to enforce the area constraint. For flows governed by the Navier-Stokes equations phase field methods have been used to investigate the dynamic dynamics of vesicles. For example, Du and colleagues [19, 20, 21] have used a penalty method with the phase field approach, but their method constrains only the total area, not the local area. Du, *et al.* [20] have stated that that although their method does not incorporate a constant differential area constraint, it is a feature of their phase field method. Another approach [18] adds an additional evolution equation for the surface tension in the phase field method. This idea was justified by thermodynamic arguments by Jamet and Misbah [23], but a consistent convergence analysis was not presented. None of these methods directly enforeces a local area constraint, *i.e.* the incompressibility of the interface, when studying a finite Reynolds number flow.

Here a level-set method which will enforce the incompressibility of the interface is developed. A projection method is presented which will determine the surface tension at each time step necessary to enforce the area constraint. This idea has the advantage over current approaches to solve the Navier-Stokes equations associated with vesicles in that a clearly defined model is presented which enforces the local area constraint. Solving for

a membrane tension in this manner to enforce the incompressibility is in spirit to several of the Stokes flow investigations noted above, but the numerical implementation and method is new. The method allows for the determination of the dynamics of a vesicle in finite Reynolds number regimes. The formulation and results will be presented for two-dimensional flows. The method described here is equally applicable to three-dimensional flows as many of the individual basic underlying techniques have been demonstrated in three dimensions, including the level set method [35], closest point method [36], fast-marching method [37], and the projection method for Navier-Stokes equations [38].

2.1. Hydrodynamic Equations

Consider a single vesicle suspended in a viscous flow, Fig. 1. Denote the entire domain as Ω. A fluid membrane, denoted as Γ, splits the domain into two exclusive regions. The region enclosed by Γ is given by Ω_1 while the rest of the domain is Ω_2 such that $\Omega = \Omega_1 \cup \Omega_2$. The fluids in Ω_1 and Ω_2 are different and have different material properties. Within each domain exists a velocity and pressure field, $\boldsymbol{u}_k$ and p_k, respectively, where $k = 1$ or 2. Both fluids are incompressible and Newtonian, leading to the following fluid model in each domain:

$$\rho_k \frac{D\boldsymbol{u}_k}{Dt} = -\nabla p_k + \nabla \cdot \left(\mu_k \left(\nabla \boldsymbol{u}_k + \nabla^T \boldsymbol{u}_k \right) \right), \tag{1}$$

$$\nabla \cdot \boldsymbol{u}_k = 0 \text{ in } \Omega_k. \tag{2}$$

The first equation is the standard momentum equation for viscous fluids where ρ is the density, $D\boldsymbol{u}/Dt$ is the convective (material) derivative, and μ is the fluid viscosity. The second equation is the standard incompressibility constraint and imposes conservation of volume in the domain.
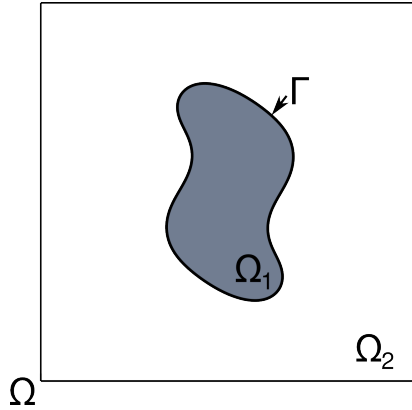

Figure 1: Sample domain, Ω, contain a fluid membrane, Γ, enclosing the vesicle, Ω_1. The second region, Ω_2, contains the external fluid.

The response of the fluid in each domain is coupled by conditions imposed on the membrane. Assume continuity of the velocity field and a jump in the hydrodynamic

stress, $\boldsymbol{\sigma}_k = -p_k \boldsymbol{I} + \mu_k \left(\nabla \boldsymbol{u}_k + \nabla^T \boldsymbol{u}_k \right)$:

$$[\boldsymbol{u}] = 0, \tag{3}$$

$$[\boldsymbol{\sigma} \cdot \boldsymbol{n}] = \boldsymbol{F}, \tag{4}$$

where $\boldsymbol{n}$ is the outward normal pointing from Ω_1 into Ω_2 and $\boldsymbol{F}$ is the force per unit area on the membrane and is derived below. In addition to this the velocity field projected onto the surface must be divergence free:

$$\nabla_s \cdot \boldsymbol{u} = 0 \qquad \text{on } \Gamma, \tag{5}$$

where $\nabla_s = \boldsymbol{P}\nabla$ the surface gradient and $\boldsymbol{P} = (\boldsymbol{I} - \boldsymbol{n} \otimes \boldsymbol{n})$ is the projection operator. This condition is enforced to ensure area-conservation and has been previously proposed [12, 25, 34].

The forces acting on the membrane can be calculated from the free energy of the membrane. Taking into account the energy discussion in Sec. 2 the free energy is written as [33]

$$E = \int_\Gamma \left(\frac{b_n}{2} \kappa^2 + \gamma \right) dA. \tag{6}$$

Here b_n is the bending rigidity, κ is the mean curvature, and γ is a membrane tension. The force on the membrane is then calculated from a variation of energy with respect to a change in membrane shape. This leads to

$$\boldsymbol{F} = b_n \left(\nabla_s^2 \kappa + \frac{1}{2} \kappa^3 \right) \boldsymbol{n} + \gamma \kappa \boldsymbol{n} - \nabla_s \gamma \boldsymbol{s}, \tag{7}$$

with $\boldsymbol{s}$ being the tangential vector and $\nabla_s^2 = \nabla_s \cdot \nabla_s$ the surface Laplacian. To complete the hydrodynamic equations a description of the interface needs to be presented.

2.2. Description of the Membrane

The level set method is implemented to track the membrane over time. A brief overview of the method will be presented below. The interested reader can refer to the review articles by Sethian and Smereka [39] or Osher and Fedkiw [40].

Consider the domain described in Sec. 2.1, with Γ being the interface separating domains Ω_1 and Ω_2. Let $\boldsymbol{x}$ be a position in space. Define an auxiliary mathematical function, $\phi(\boldsymbol{x}, t)$, in the entire domain Ω such that at any time t the interface $\Gamma(t)$ can be determined by

$$\Gamma(t) = \{\boldsymbol{x} : \phi(\boldsymbol{x}, t) = 0\} . \tag{8}$$

This simply states that the zero of the function ϕ corresponds to the interface. According to convention the level set function is $\phi < 0$ in Ω_1 and $\phi > 0$ in Ω_2. While any function which satisfies this description may be used, for stability reasons the level set function is restricted to signed distance functions. The major advantage of such an implicit representation is that large changes in the interface, such as the merging of bodies or the pinching off of a portion of a body, can be handled naturally without the need for

complex remeshing [41, 42]. Using this representation the outward normal and mean curvature can be calculated as

$$\boldsymbol{n} = \frac{\nabla \phi}{\|\nabla \phi\|}, \tag{9}$$

$$\kappa = \nabla \cdot \frac{\nabla \phi}{\|\nabla \phi\|}. \tag{10}$$

The motion of the interface due to an underlying flow field, $\boldsymbol{u}$, carries the associated level set function as if ϕ was a material property. Accordingly the motion of the level set function is described by

$$\frac{\partial \phi}{\partial t} + \boldsymbol{u} \cdot \nabla \phi = 0. \tag{11}$$

Material properties at any point $\boldsymbol{x}$ in the domain Ω can be determined by the level set value at $\boldsymbol{x}$. For example, let the density in the domain be given by ρ_1 and ρ_2 for Ω_1 and Ω_2, respectively. The density at any point can be calculated as $\rho(\boldsymbol{x}) = \rho_1 + (\rho_2 - \rho_1)H(\phi(\boldsymbol{x}))$, where $H(y)$ is the Heaviside function such that $H(y) = 0$ for $y < 0$, $H(y) = 1$ for $y > 0$, and $H(0) = 0.5$.

2.3. Single-Fluid Model

Using the interface description given in Sec. 2.2 it is now possible to write the hydrodynamic equations (1)-(5) and (7) in the single-fluid formulation. Following the work of Chang, *et al.* [43] the membrane conditions (3) and (4) can be written as body-force terms in the momentum equation. These contributions are localized around the membrane through the use of a Dirac-delta function, $\delta(y) = dH(y)/dy$. This leads to the following system:

$$\rho \frac{D\boldsymbol{u}}{Dt} = -\nabla p + \nabla \cdot \left(\mu \left(\nabla \boldsymbol{u} + \nabla^T \boldsymbol{u} \right) \right)$$
$$+ \delta(\phi) \left(|\nabla \phi| \nabla_s \gamma - \gamma \kappa \nabla \phi \right) + b_n \delta(\phi) \left(\nabla_s^2 \kappa + \frac{1}{2} \kappa^3 \right) \nabla \phi \tag{12}$$

$$\nabla \cdot \boldsymbol{u} = 0 \text{ in } \Omega \tag{13}$$

$$\nabla_s \cdot \boldsymbol{u} = 0 \text{ on } \Gamma. \tag{14}$$

Note that this system is valid in the entire domain. Material properties such as density and viscosity are calculated through the use of the level set function. To complete the formulation of the problem the velocity is specified at infinity, $\boldsymbol{u}_\infty$. For the special case of a two-dimensional shear flow this results in a far-field condition of $\boldsymbol{u}_\infty = \dot{\gamma}(y, 0)$, where $\dot{\gamma}$ is the shear rate and y is the vertical location.

2.4. Normalization

Dimensionless units for two-dimensional vesicles can be introduced by following the analysis of ref. [44]. Consider a vesicle of encapsulated area A with a membrane arc length L. A characteristic length is defined as the radius of a circle with a perimeter of L: $R_0 = L/2\pi$. The bending rigidity, b_n, sets the energy scale. In combination with the the bulk viscosity, μ_2, and R_0 a characteristic time can be defined as $\tau = \mu_2 R_0^3 / b_n$.

All velocities are scaled as $u_0 = R_0/\tau$. The membrane tension is scaled by the quantity $\gamma_0 = (\rho_2 b_n^2)/(\mu_2^2 R_0^3)$. This results in the following normalized Navier-Stokes equation:

$$\hat{\rho}\frac{D\hat{\boldsymbol{u}}}{Dt} = - \nabla\hat{p} + \frac{1}{Bn}\nabla \cdot \left(\hat{\mu}\left(\nabla\hat{\boldsymbol{u}} + \nabla^T\hat{\boldsymbol{u}}\right)\right)$$
$$+ \delta(\phi)\left(|\nabla\phi|\nabla_s\hat{\gamma} - \hat{\gamma}\hat{\kappa}\nabla\phi\right) + \frac{1}{Bn}\delta(\phi)\left(\nabla_s^2\hat{\kappa} + \frac{1}{2}\hat{\kappa}^3\right)\nabla\phi, \tag{15}$$

where dimensionless numbers are denoted with a hat. Note that $\hat{\rho} = \rho/\rho_2$ and $\hat{\mu} = \mu/\mu_2$ are the density and viscosity normalized by their counterparts in the bulk fluid, and $Bn = (\rho_2 b_n)/(R_0 \mu_2^2)$ is a bending number giving the relative strength of the bending effects. This number can also be thought of as bending capillary number relating the bending to surface tension effects, $Bn = \gamma_0 R_0^2/b_n$, using the definition of γ_0 above [12, 14]. From this point forward the hat notation is dropped with the understanding that all quantities are normalized.

Two-dimensional vesicles are classified by two quantities, a viscosity ratio $\eta = \mu_1/\mu_2$ and the reduced area, $\nu = A/\pi R_0^2 = 4A\pi/L^2$. The reduced area measures how much lower the encapsulated area is compared to a circle with the same perimeter. The shear rate is normalized with the characteristic time, $\chi = \dot{\gamma}\tau = \dot{\gamma}\mu_2 R_0^3/b_n$, giving a dimensionless velocity condition of $\boldsymbol{u}_\infty = \chi(y, 0)$ at infinity. Under shear flow conditions the Reynolds number is given by $Re = \chi Bn$.

3. Numerical Implementation

In this section the numerical implementation of the level set and fluid equations are discussed. The methods described here will be first-order in time and second-order in space. Higher order implementations are possible.

3.1. Level Set Discretization

The motion of the membrane is modeled by the advection of the level set function, Eq. (11). Due to the nature of the flow and its dependence on high-order derivatives of the level set function the ϕ field must be smooth and accurate at all times. This is accomplished using augmented level set methods.

A gradient-augmented level set scheme introduced by Nave et. al is used to advance the membrane forward in time [35]. In this method both the level set function ϕ and its gradient, $\boldsymbol{\psi} = \nabla\phi$, are advanced forward by solving the following evolution equations in Lagrangian form:

$$\frac{D\phi}{Dt} = 0, \tag{16}$$

$$\frac{D\boldsymbol{\psi}}{Dt} = -\nabla\boldsymbol{u} \cdot \boldsymbol{\psi}, \tag{17}$$

where D/Dt represents the Lagrangian (material) derivative. To advance the membrance forward in time material particles are traced backwards in time from a grid point at time t_{n+1} to their departure location at time t_n. Using accurate interpolation techniques on

the values at time t_n the new updated values at time t_{n+1} can be obtained. To first order in time the semi-discrete form of Eqs. (16) and (17) is written as

$$\boldsymbol{x}_d = \boldsymbol{x} - \Delta t \boldsymbol{u}_n, \tag{18}$$

$$\phi_{n+1} = \phi_n\left(\boldsymbol{x}_d\right), \tag{19}$$

$$\boldsymbol{\psi}_{n+1} = \left(\boldsymbol{I} - \Delta t \nabla \boldsymbol{u}_n\right) \cdot \boldsymbol{\psi}_n\left(\boldsymbol{x}_d\right). \tag{20}$$

The values of ϕ and $\boldsymbol{\psi}$ at the departure location $\boldsymbol{x}_d$ are calculated through the use of a Hermite bicubic interpolant defined over a cell surrounding the point $\boldsymbol{x}_d$. The level set and gradient values are already available and do not need to be calculated. To fully define the Hermite interpolant the second-order derivatives ϕ_{xy} is defined as an average of the derivatives of ψ_x and ψ_y in the y- and x-directions, respectively. The Navier-Stokes solver below does not provide an explicit updating rule for the velocity deformation matrix $\nabla \boldsymbol{u}_n$. Instead the matrix is approximated using standard finite difference approximations of the velocity derivatives.

To aid in the stability of the method periodic reinitialization is required. In reinitialization a current level set function is replaced with a signed distance function having the same zero contour. In [45] a new extension to the standard fast marching method is shown. Let ϕ represent a signed distance function which has the property $\|\nabla\phi\| = 1$. The fast marching method is an optimal method for solving equations of this type [46]. The idea is to enforce $\|\nabla\phi\| = 1$ at every grid point by using upwind finite differences. This upwinding induces a causality in the order in which nodes can be updated. Let the grid point $\boldsymbol{y}$ be farther away from a given interface than the grid point $\boldsymbol{x}$. Thus we have $\phi(\boldsymbol{x}) < \phi(\boldsymbol{y})$. Due to the upwing scheme the value at $\boldsymbol{x}$ needs to be updated before the value at $\boldsymbol{y}$. The use of an efficient sorting algorithm controls the order in which nodes are updated. More information about the basic fast marching method can be found in references [37, 46, 47, 48].

A limitation of using FMM for reinitialization is that quantities which depend on high derivates of the level set function are not smooth due to the strictly one-sided nature of the update scheme. To address this the following augmented system is updated at every computational node:

$$\nabla\phi \cdot \nabla\phi = 1, \tag{21}$$

$$\nabla\left(\nabla\phi \cdot \nabla\phi\right) = 0, \tag{22}$$

$$\nabla\nabla\left(\nabla\phi \cdot \nabla\phi\right) = 0. \tag{23}$$

In two dimensions this results in six unique equations at every grid point for up to second order derivatives of the level set, ϕ, ψ, and $\nabla\psi$. Replacing derivatives with finite difference approximations results in a set of nonlinear equations to be solved at every grid point. While this nonlinear system is larger than the systems in other fast marching methods such as ref. [46] the additional solution cost is small.

3.2. Hydrodynamic Time Discretization

In addition to advecting the level set function a scheme is needed to solve for the fluid field. Here a novel semi-Lagrangian, semi-implicit, 4-step projection method is developed

to accomplish this. Information regarding standard projection methods for the Navier-Stokes equations can be found in references [38, 49, 50] while the semi-Lagrangian method is outlined in ref. [51].

A major difficulty in solving the Navier-Stokes equations is the application of the divergence-free conditions. In this work there are two conditions which need to be satisfied, Eq. (13) and (14). Consider solving the Navier-Stokes equations in the computational domain Ω with a boundary of $\partial\Omega$. The 4-step projection method here is written as:

$$\rho\frac{\boldsymbol{a} - \boldsymbol{u}_d}{\Delta t} = \frac{1}{Bn}\nabla\cdot\left(\mu\nabla^T\boldsymbol{u}_n\right) + \frac{1}{Bn}\left(\nabla_s^2\kappa + \frac{1}{2}\kappa^3\right)\delta(\phi)\nabla\phi, \tag{24}$$

$$\rho\frac{\boldsymbol{b} - \boldsymbol{a}}{\Delta t} = -\nabla p_{n+1} \text{ with } \nabla\cdot\boldsymbol{u}_{n+1} = 0 \text{ in } \Omega, \tag{25}$$

$$\rho\frac{\boldsymbol{c} - \boldsymbol{b}}{\Delta t} = \frac{1}{Bn}\nabla\cdot\left(\mu\nabla\boldsymbol{c}\right), \tag{26}$$

$$\rho\frac{\boldsymbol{u}_{n+1} - \boldsymbol{c}}{\Delta t} = \delta(\phi)\left(|\nabla\phi|\nabla_s\gamma_{n+1} - \gamma_{n+1}\kappa\nabla\phi\right) \text{ with } \nabla_s\cdot\boldsymbol{u}_{n+1} = 0 \text{ on } \Gamma. \tag{27}$$

where Δt is the current time step and $\boldsymbol{a}, \boldsymbol{b}, \boldsymbol{c}$ are intermediate velocity fields.

The first step, Eq. (24), calculates an explicit intermediate velocity field, $\boldsymbol{a}$, using the non-linear viscous portion of the momentum equation and the contribution from the bending of the membrane. The convective derivative is not split. Instead the departure velocity at time t_n, $\boldsymbol{u}_d$, is used to explicitly calculate this derivative. Consider a fluid particle located at the grid point $\boldsymbol{x}_{n+1}$ at time t_{n+1}. The departure location of this particle at time t_n is denoted as $\boldsymbol{x}_d$. As in level set advancement to first order this departure location can be calculated as $\boldsymbol{x}_d = \boldsymbol{x}_{n+1} - \Delta t\boldsymbol{u}_n$. In almost all instances this departure location will not land on a grid point at time t_n so an accurate interpolation scheme, such as a bicubic interpolation function, is needed to calculate $\boldsymbol{u}_d = \boldsymbol{u}_n(\boldsymbol{x}_d)$.

The second step, Eq. (25), is the standard pressure-projection step to enforce the incompressibility of the velocity field. Further information regarding this step, including the necessary boundary conditions and solution methods can be found in references [38, 49]. Next a semi-implicit update is performed, Eq. (26), to ensure the stability of the method. During the semi-implicit update the domain boundary, $\partial\Omega$, is split into a portion with Dirilicht velocity boundary conditions, $\partial\Omega_d$, and a portion with periodic boundary conditions, $\partial\Omega_p$, such that $\partial\Omega = \partial\Omega_d\bigcup\partial\Omega_p$. For example, to simulate simple shear on a square domain a known velocity can by applied in the y-direction while periodicity can be enforced in the x-direction. As long as the period of the computational domain is large the numerical results should simulate well the problem of an isolated vesicle. For smaller periods an effect will be seen and this will be mentioned when present in the numerical results. Finally, Eq. (27), calculates the needed membrane tension, γ_{n+1}, to ensure that the velocity on the membrane is surface area conserving. This step will be described in more detail below.

3.2.1. Surface-Projection Method

Focus will now shift to the surface area conserving step of the projection method described above. Combine the expressions in Eq. (24)-(27) to obtain

$$\rho\frac{\boldsymbol{u}_{n+1} - \boldsymbol{a}}{\Delta t} = -\nabla p_{n+1} + \frac{1}{Bn}\nabla\cdot\left(\mu\nabla\boldsymbol{u}_{n+1}\right) + \delta(\phi)\left(|\nabla\phi|\nabla_s\gamma_{n+1} - \gamma_{n+1}\kappa\nabla\phi\right). \tag{28}$$

On the interface, Γ, Eq. (14) is applied and the result is rearranged. To ensure all scalars are explicit defined the pressure and velocity field values at time t_{n+1} are replaced by the respective values at time t_n. This leads to the following equation:

$$\delta(\phi)\nabla_s \cdot (\gamma_{n+1}\kappa\nabla\phi - |\nabla\phi|\nabla_s\gamma_{n+1}) = \nabla_s \cdot \left(\rho\frac{\boldsymbol{a}}{\Delta t} - \nabla p_n + \frac{1}{Re}\nabla \cdot (\mu\nabla\boldsymbol{u}_n)\right). \quad (29)$$

This equation is only valid on the interface. Instead of discretizing the interface the closest point method [36, 52] is utilized to solve for the tension in a small region surrounding the interface. Consider the computational region Ω_γ near the interface. Modify Eq. (29) by dropping the $\delta(\phi)$ term and assume that $|\nabla\phi| = 1$ everywhere. This last condition should be approximately true if the level set field is maintained as a signed distance function. Also note that $\nabla_s f \cdot \boldsymbol{n} = 0$ for any scalar f defined on the interface and that $\kappa = \nabla_s \cdot \boldsymbol{n}$. Thus, the PDE of interest is now

$$\gamma_{n+1}\kappa^2 - \nabla_s^2\gamma_{n+1} = \nabla_s \cdot \left(\rho\frac{\boldsymbol{a}}{\Delta t} - \nabla p_n + \frac{1}{Bn}\nabla \cdot (\mu\nabla\boldsymbol{u}_n)\right). \quad (30)$$

The main idea behind the closest point method is to replace an intrinsic PDE with one valid in the embedding space by replacing quantities, such as tension, by values on the interface. Let $\boldsymbol{x}$ be a point away from the interface Γ and let $\boldsymbol{cp}(\boldsymbol{x})$ be the closest point on Γ to $\boldsymbol{x}$. It follows that points in the normal direction away from the interface will have the same closest point location. This leads to the following two principles on the interface [36, 52]: $\nabla f(\boldsymbol{cp}(\boldsymbol{x})) = \nabla_s f$ for a scalar f and $\nabla \cdot \boldsymbol{v} = \nabla_s \cdot \boldsymbol{v}$ for a vector field tangent to the interface. These two principles also give the relationship $\nabla \cdot \nabla f(\boldsymbol{cp}(\boldsymbol{x})) = \nabla_s \cdot \nabla_s f$ on the interface. Using these relationships, Eq. (30) can be written in Eulerian form at a point $\boldsymbol{x}$ as

$$\gamma_{n+1}(\boldsymbol{cp}(\boldsymbol{x}))\kappa^2 - \nabla^2\gamma_{n+1}(\boldsymbol{cp}(\boldsymbol{x})) = \nabla \cdot \left(\boldsymbol{P}\left(\rho\frac{\boldsymbol{a}}{\Delta t} - \nabla p_n + \frac{1}{Re}\nabla \cdot (\mu\nabla\boldsymbol{u}_n)\right)\right), \quad (31)$$

It is now possible to discritize Eq. (31) using standard finite difference discretizations. Consider the 2nd-order discretization of the right hand side of Eq. (31) at a grid point $\boldsymbol{x}_{i,j}$ on a 2D Cartesian grid with grid spacing h: $(\gamma(\boldsymbol{cp}(\boldsymbol{x}_{i,j}))(4 + \kappa_{i,j}^2) - \gamma(\boldsymbol{cp}(\boldsymbol{x}_{i-1,j})) - \gamma(\boldsymbol{cp}(\boldsymbol{x}_{i+1,j})) - \gamma(\boldsymbol{cp}(\boldsymbol{x}_{i,j-1})) - \gamma(\boldsymbol{cp}(\boldsymbol{x}_{i,j+1})))/h^2$. Typically the closest point location will not lie on a grid point. The values $\gamma(\boldsymbol{cp}(\boldsymbol{x}_{i,j}))$ are thus replaced by an interpolation stencil, $I_\gamma(\boldsymbol{cp}(\boldsymbol{x}_{i,j}))$, which is an interpolation polynomial evaluated at the closest point. Given a pth-order spatial discretization of the underlying PDE and an interpolation order of $q \geq p + 1$ the overall order of the closest point discretization will be p^{th}-order [36, 53]. In this work second-order accurate derivative approximations are used and thus the interpolant chosen is 3rd-order (bicubic).

There are two major advantages of the closest point formulation given above. First, the resulting computational domain, Ω_γ, can be wholly determined by the interpolation stencil. All of the grid points in the PDE stencil are replaced by their closest point interpolation stencil. Thus the domain Ω_γ consists of those grid points needed to create the interpolation stencils.

The second advantage of the closest point representation is that no artificial boundary conditions are needed to solve the resulting PDE. Consider a discretization where the

10

grid point $\boldsymbol{x}_{i+1,j}$ is not in the domain Ω_γ. As the value at $\boldsymbol{x}_{i+1,j}$ is replaced with the interpolation stencil, $I_\gamma(\boldsymbol{cp}(\boldsymbol{x}_{i+1,j}))$, which is contained within Ω_γ, no additional information is needed.

4. Verification of Methods

In this section the methods outlined above are verified by presenting convergence results.

4.1. Calculation of the Tension

To verify the membrane tension calculated using Eq. (30) convergence studies using a known shape and an imposed velocity field are performed. The three shapes considered here are an ellipse with a minor axis of 3/5 and a major axis of 2, a Cassini Oval with the implicit function of $\left((x-a)^2 + y^2\right)\left((x+a)^2 + y^2\right) = b^4$ with parameters $a = 1$ and $b = 1.01$, and a five-point star given by the parametric equation $r(\theta)\left(\cos(\theta), \cos(\theta)\right)$, where $r(\theta) = 1 + \sin(5\theta)/4$, see Fig. 2. In the first check mean curvature flow is prescribed on the interface, $\boldsymbol{u} = \kappa\boldsymbol{n}$, resulting in $\nabla_s \cdot \boldsymbol{u} = \kappa^2$. This results in an analytic solution of $\gamma = 1$ on the membrane. The membrane tension is calculated using the closest point method outlined above. To compare to the analytic solution bicubic interpolation is used to determine the calculated membrane tension on the interface. These interpolated values are then compared to the analytic solution in both the l^2 and l^∞ norms, Fig. 3. In both cases convergence on the order of h^2 is observed.
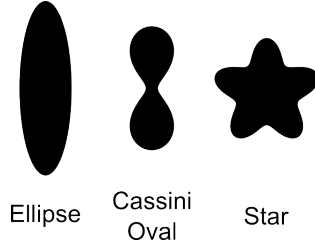
Figure 2: The shapes used for verification of the tension calculation. There is an ellipse with a minor axis of 3/5 and major axis of 2, a Cassini Oval with parameters $a = 1$ and $b = 1.01$, and a star shape given by a parametric equation of $r(\theta)\left(\cos(\theta), \cos(\theta)\right)$, where $r(\theta) = 1 + \sin(5\theta)/4$.

Next turn to the case where an analytic solution does not exist. Consider a membrane with a prescribed velocity of $\boldsymbol{u} = \boldsymbol{n}$, resulting in $\nabla_s \cdot \boldsymbol{u} = \kappa$. Solve Eq. (30) using this prescribed velocity. The exact solution is obtained by discretizing the one-dimensional differential equation $\gamma\kappa^2 - d_{ss}\gamma = \kappa$, where s is arc-length, on the interface. Assuming periodicity a very accurate membrane tension can be calculated. The exact tension and the tension obtained using our projection-operator are shown Fig. 4(a) for the star-shape, while the convergence of the solution is shown in Fig. 4(b). Convergence of both norms is 2nd order.
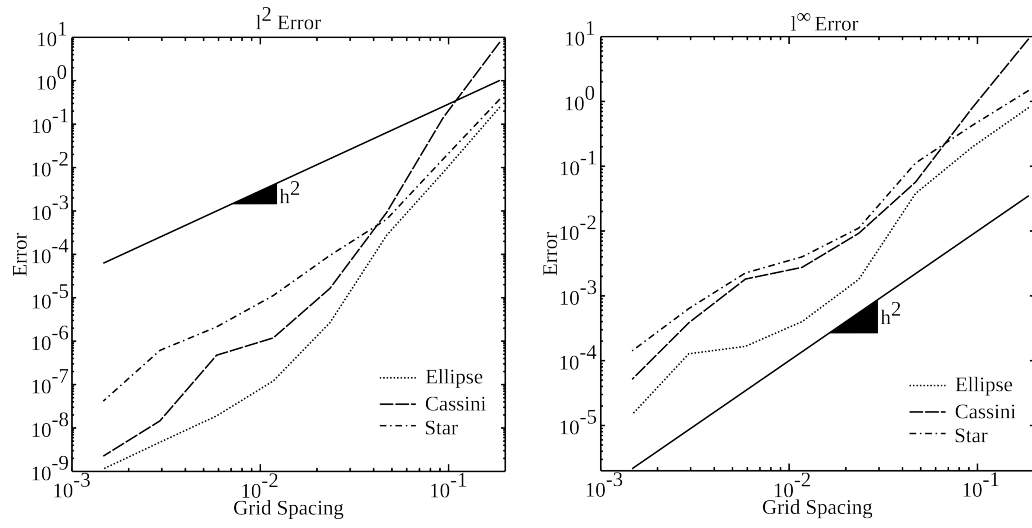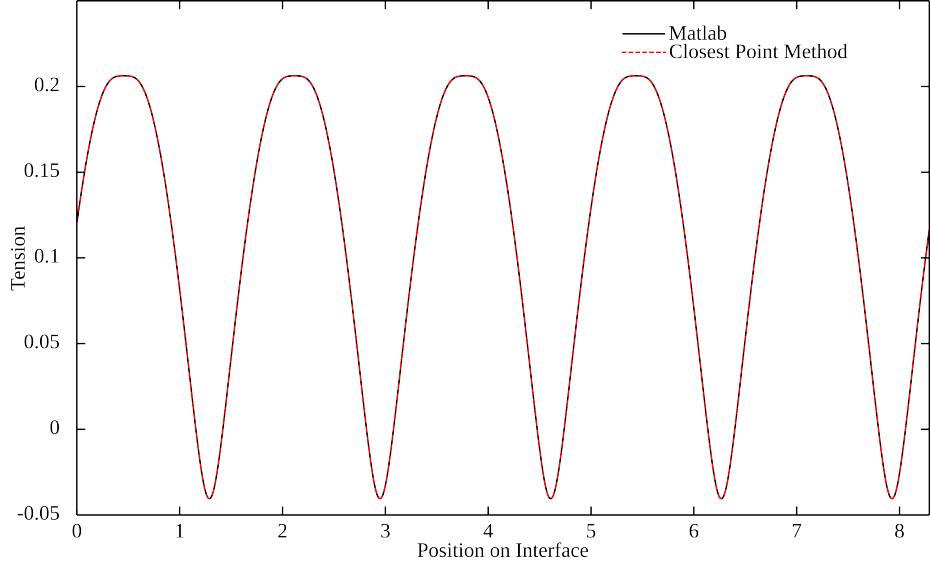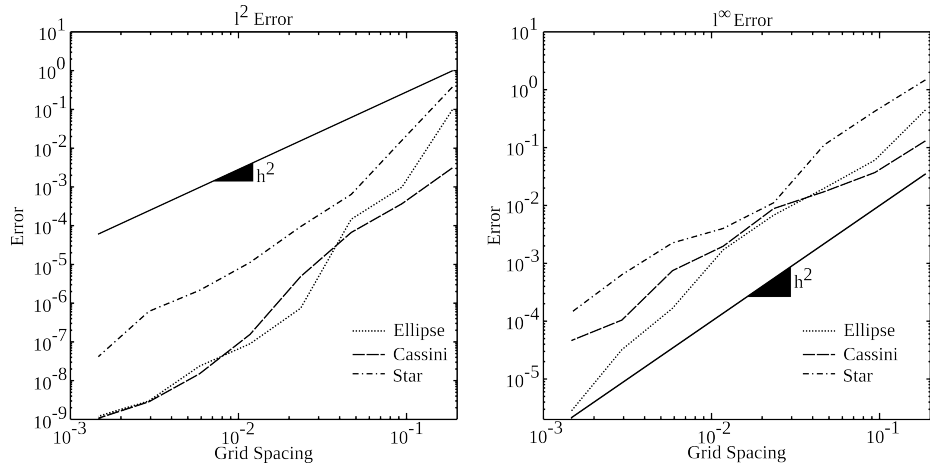
Figure 3: Convergence of the surface-divergence operator with a prescribed velocity of $\boldsymbol{u} = \kappa\boldsymbol{n}$. The overall convergence order is at least 2nd-order in both the l^2 and l^∞ norm cases.

(a) Membrane Tension on Interface

(b) Error versus Grid Spacing

Figure 4: Convergence of the surface-divergence operator with a prescribed velocity of $\boldsymbol{u} = \boldsymbol{n}$. (a) The membrane tension computed by solving the PDE on the interface is compared to the tension computed using the closest point method for the five-point star shape. (b) The overall convergence is at least 2nd-order 2 in both the l^2 and l^∞ norm cases.

14

4.2. Spatial and Temporal Convergence

The spatial and temporal convergence of the overall scheme is now presented. Two test cases are considered: a vesicle evolving due to purely bending effects and a vesicle exposed to an externally applied shear flow. As a first test case consider an initially elliptical vesicle with a major axis of 2.15 and a minor axis of 0.61 with $\nu = 0.6$ and $\eta = 1$ placed in a stationary ($\chi = 0$) fluid. The computational domain is a box of size $[-3, 3] \times [-3, 3]$ with zero velocity prescribed on the domain boundary. The vesicle will relax to reduce the bending energy. Here two bending numbers, $Bn = 10^{-4}$ and $Bn = 1$, are considered. Note that despite the lack of any external forcing, the system observes fluid flow due to the bending eneregy of the membrane.

The temporal convergence of the scheme for the bending energy relaxation case is presented in Figs. 5 and 6. Here the grid spacing is fixed at $h = 6 \times 2^{-7}$ and the time step is varied. As no analytic solution exists results for time steps $\Delta t > \Delta t_{min}$ are compared to the result using $\Delta t_{min} = 2 \times 10^{-5}$. Results are compared at times of $t = 0.5$. The method demonstrates first order convergence in time for this test case.
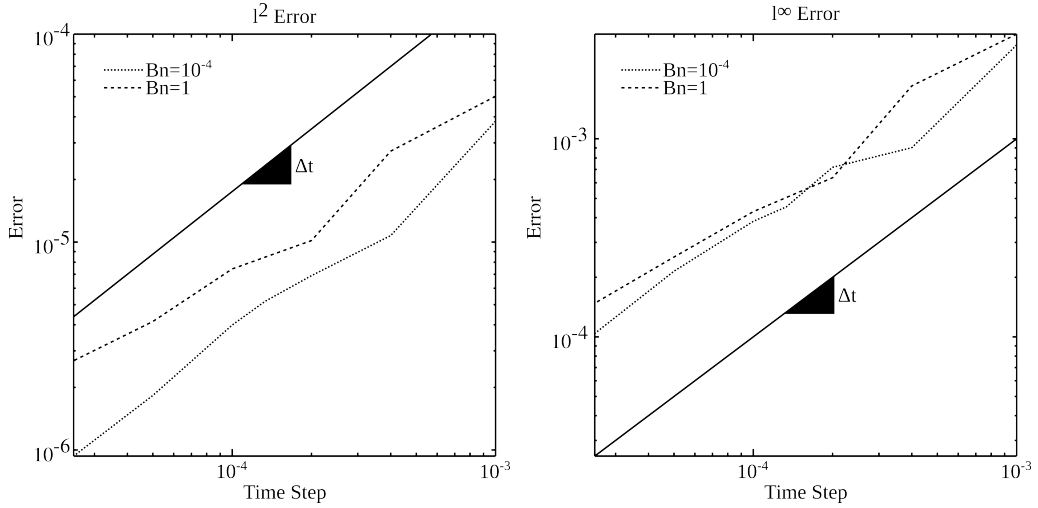
Figure 5: Convergence of the level set function versus time step for a vesicle reaching an equilibrium shape with $Bn = 10^{-4}$ and $Bn = 1$. Results from a large time step are compared to results using $\Delta t = 2 \times 10^{-5}$. Results indicate approximately first order convergence in both norms.

The second test case considered is a vesicle undergoing a shear flow of strength $\chi = 1$. The same vesicle with $\nu = 0.6$ and $\eta = 1$ is utilized and placed in a computational domain of size $[-3, 3] \times [-3, 3]$. The domain is periodic in the x-direction and has Dirilicht boundary conditions in the y-direction. As before the simulation is run up to a time of $t = 0.5$ for various time steps. All results are compared to a simulation performed with a time step of $\Delta t = 2 \times 10^{-5}$. Convergence for both the level set and the velocity field is seen in Fig. 7 and 8. Again first order convergence in time is observed.

Spatial convergence is now considered. The time step is set at $\Delta t = 0.1h^2$ where h is the grid spacing. With this time step restriction it is expected that the method should show second order convergence with respect to grid spacing. As with the temporal
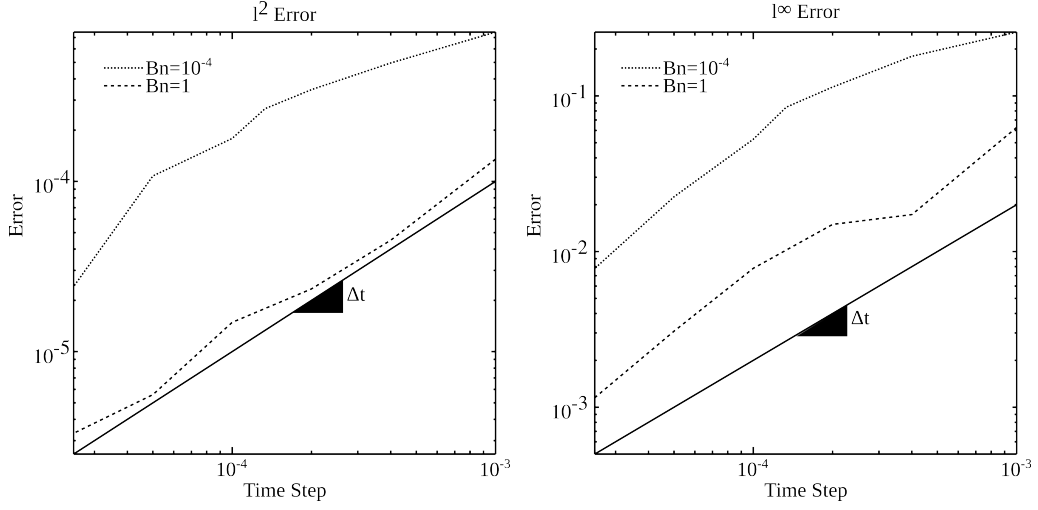
15

Figure 6: Convergence of the velocity field versus time step for a vesicle reaching an equilibrium shape with $Bn = 10^{-4}$ and $Bn = 1$. Results from a large time step are compared to results using $\Delta t = 2 \times 10^{-5}$. Results indicate approximately first order convergence in both norms.
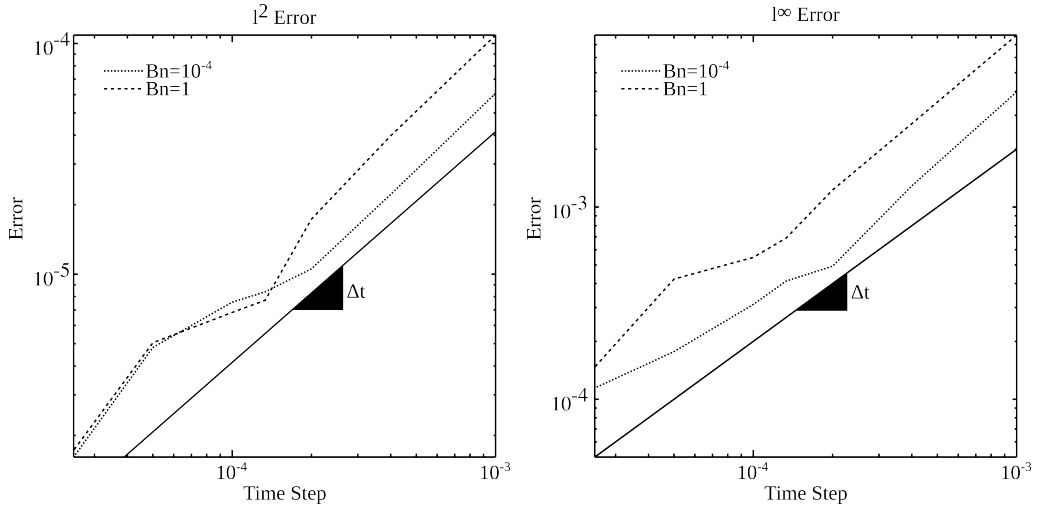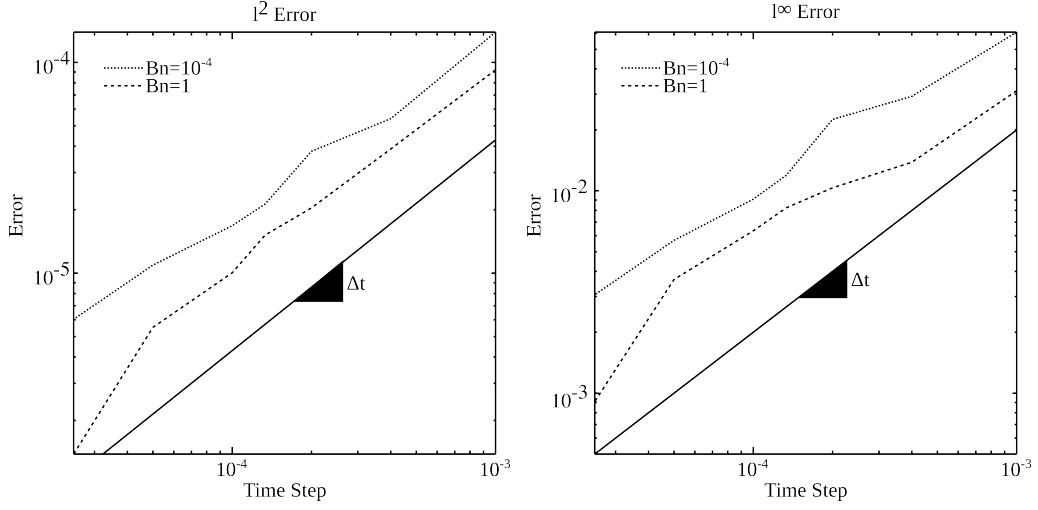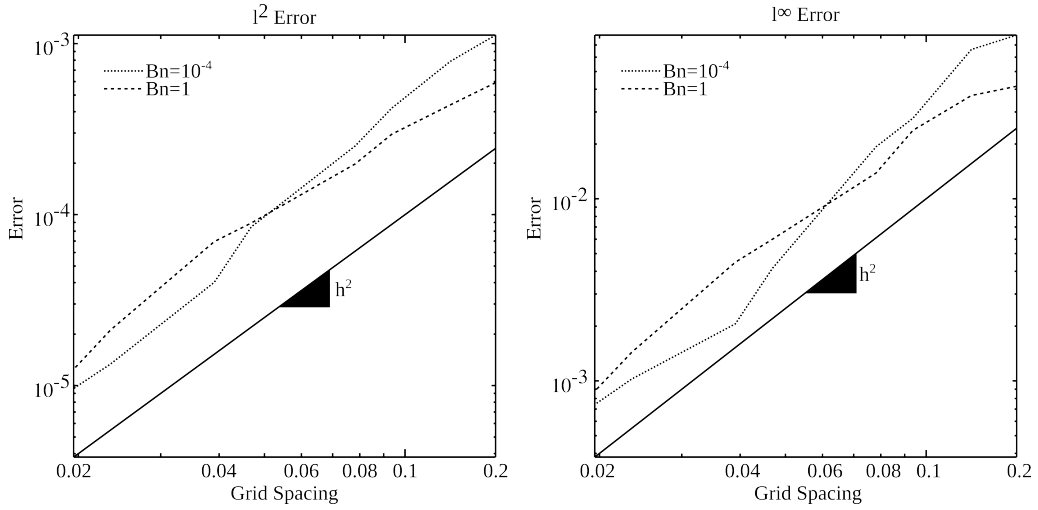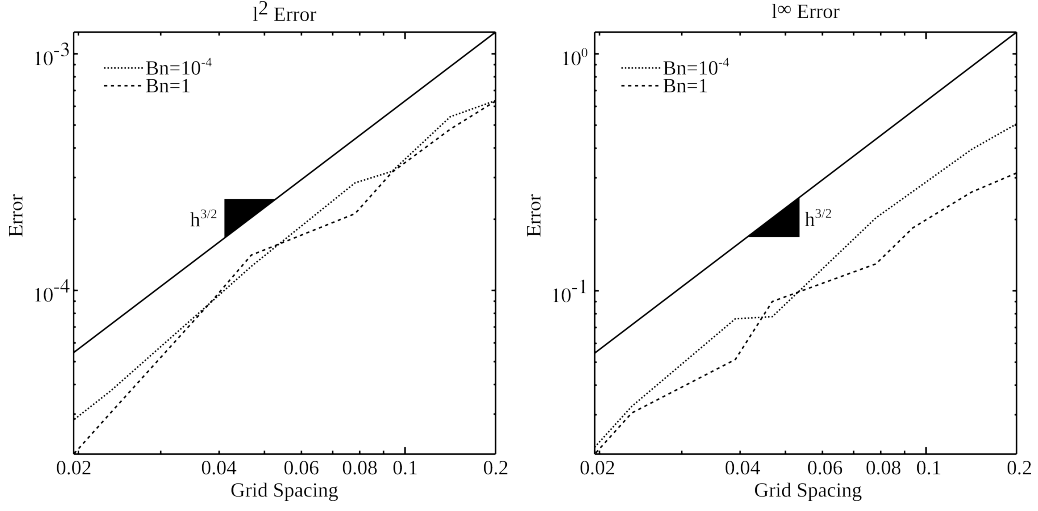

Figure 7: Convergence of the level set function versus time step for a vesicle in a shear flow of strength $\chi = 1$ with $Bn = 10^{-4}$ and $Bn = 1$. Results from a large time step are compared to results using $\Delta t = 2 \times 10^{-5}$. Results indicate approximately first order convergence in both norms.

convergence study two cases are considered, the relaxation due to bending and an induced shear flow. The result from the first case is shown in Figs. 9 and 10. The convergence of the level set function demonstrates the expected second-order convergence. The fluid field demonstrates a convergence order of 3/2.

16

Figure 8: Convergence of the velocity field versus time step for a vesicle in a shear flow of strength $\chi = 1$ with $Bn = 10^{-4}$ and $Bn = 1$. Results from a large time step are compared to results using $\Delta t = 2 \times 10^{-5}$. Results indicate approximately first order convergence in both norms.

Figure 9: Convergence of the level set function versus grid spacing for a vesicle reaching an equilibrium shape with $Bn = 10^{-4}$ and $Bn = 1$. Results are compared to a solution from a mesh equivalent to 1024×1024 (grid spacing of 6×2^{-10}). Results indicate second-order convergence in both norms.

The resultant convergence for the shear flow test case is show in Figs 11 and 12. The results again indicate second order convergence in the level set function and convergence on the order of 3/2 for the velocity fluid field.

17

Figure 10: Convergence of the velocity versus grid spacing for a vesicle reaching an equilibrium shape with $Bn = 10^{-4}$ and $Bn = 1$. Results are compared to a solution from a mesh equivalent to 1024x1024 (grid spacing of 6×2^{-10}). Results indicate convergence on the order of 3/2 in both norms.
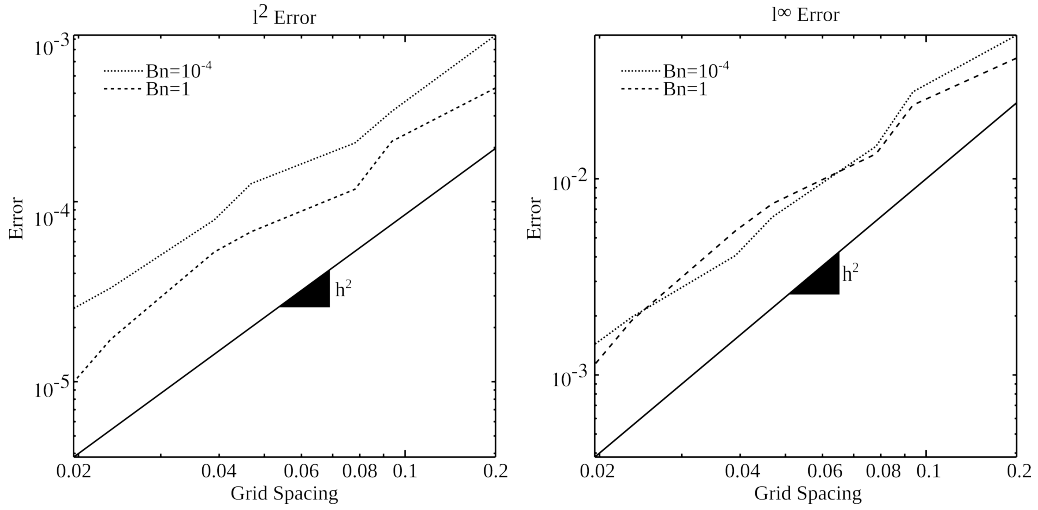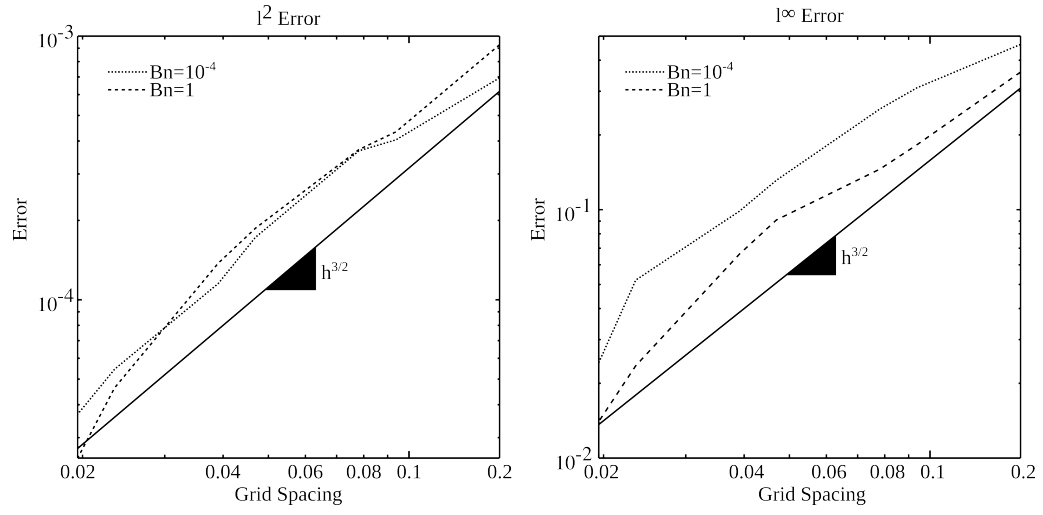

Figure 11: Convergence of the level set function versus grid spacing for a vesicle in a shear flow of strength $\chi = 1$ with $Bn = 10^{-4}$ and $Bn = 1$. Results are compared to a solution from a mesh equivalent to 1024×1024 (grid spacing of 6×2^{-10}). Results indicate second-order convergence in both norms.

18

Figure 12: Convergence of the velocity versus grid spacing for a vesicle in a shear flow of strength $\chi = 1$ with $Bn = 10^{-4}$ and $Bn = 1$. Results are compared to a solution from a mesh equivalent to 1024x1024 (grid spacing of 6×2^{-10}). Results indicate convergence on the order of $3/2$ in both norms.

4.3. Conservation of Enclosed Area and Membrane Length

As an example of the conservation properties of the method the enclosed area and membrane length is tracked over time for an initially elliptical vesicle with a reduced area of $\nu = 0.6$. The vesicle is placed in a square domain with zero velocity boundary conditions and allowed to relax to an equilibrium shape under the influence of bending with $Bn = 10^{-4}$. Example equilibrium shapes for various reduced areas are shown in Fig. (15). The resultant area and length, shown in Fig. (13), shows excellent convervation in both the enclosed area and membrane length is obtained. For comparison the evolution of the same vesicle without using Eq. (27) is also calculated. In this situation the vesicles behaves as a droplet and evolves towards a circle.

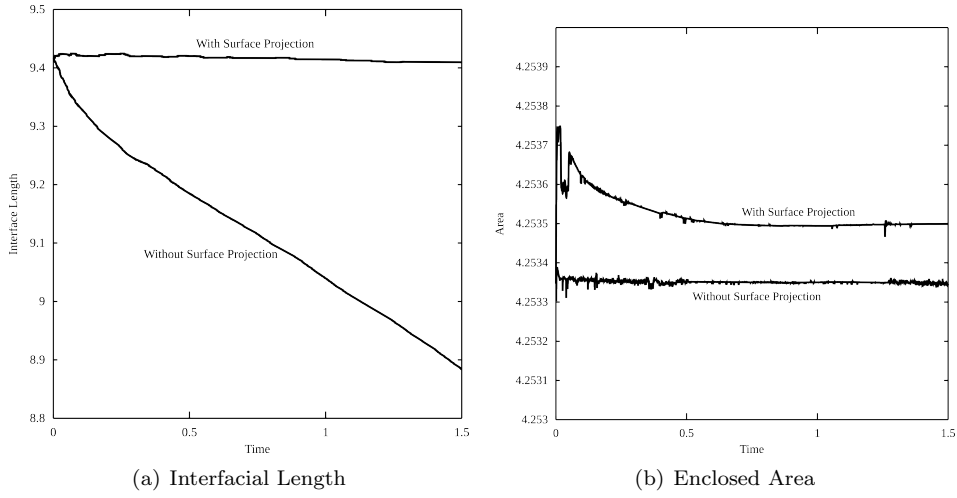(a) Interfacial Length   (b) Enclosed Area

Figure 13: The enclosed area and interfacial length of a relaxing vesicle of reduced area $\nu = 0.6$. Two cases are considered: with the surface projection method obtain tension as described in Sec. (3.2.1, and the no tension.

20

5. Results: Single Vesicle

In this section results utilizing the numerical scheme outlined above are presented. Multiple vesicle results are shown in the next section. Unless otherwise stated the fluid is initially stationary and any boundary conditions, such as shear flow or pressure gradient, are applied instantaneously at time $t = 0$.

5.1. Minimization of Bending Energy

A vesicle with $Bn \neq 0$ placed in a stationary fluid ($\chi = 0$) will attempt to minimize the bending energy of the membrane. In a surfactant free bubble or droplet with a uniform tension this would result in a circle. Due to the interface length constraint the equilibrium shape for a vesicle will not be a circle, but a biconcave shape. Consider the shape given in Fig. 14 at $t = 0$. This shape has a reduced area of $\nu = 0.3$ and is allowed to evolve in a stationary viscous fluid using the parameters $Bn = 10^{-3}$ and $\eta = 1$. If the characteristic velocity for this instance is defined as $u_0 = R_0/\tau$, where τ is the characteristic time defined above, then the Reynolds number is equal to the Bending number, $Re = Bn$. The relaxation of the shape and the bending energy over time are presented in Fig. 14. The equilibrium shapes for vesicles of various reduced areas has also been calculated and are shown in Fig. 15.
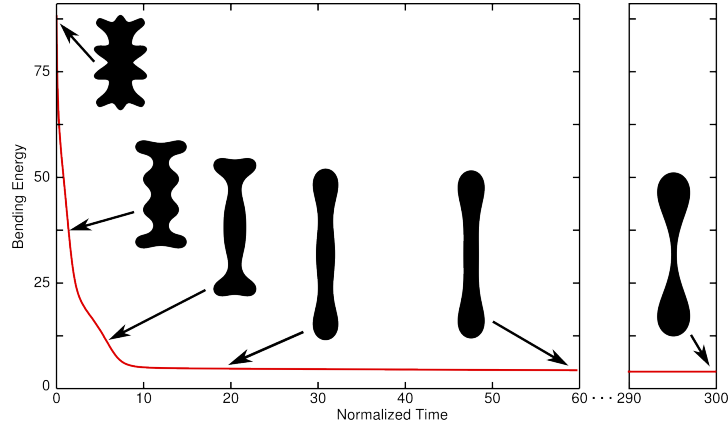

Figure 14: Bending energy as a function of dimensionless time. The maximum time step is 0.1.
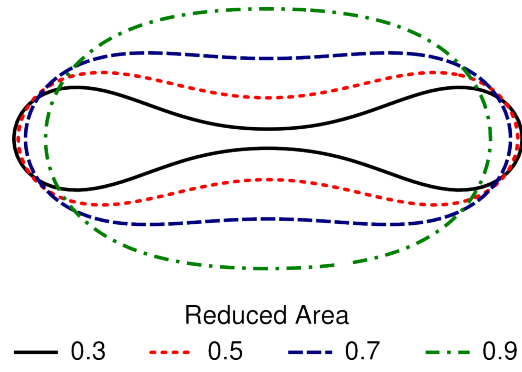
21

Figure 15: Equilibrium shapes which minimize the bending energy. These were computed in a domain of size $[-3, 3] \times [-3, 3]$ on a grid with minimum grid spacing of 6×2^{-9} and a maximum time step of 10^{-2}.

5.2. Shear Flow

Now consider a single vesicle suspended in a simple shear flow, where $\boldsymbol{u}_\infty = (\chi y, 0)$ is prescribed far from the vesicle. If the viscosity ratio between the interior and exterior fluids is below a critical value the vesicle will undergo what is called tank-treading [3, 12, 54]. This behavior is typified by the vesicle reaching an equilibrium inclination angle with respect to the external flow direction. This type of behavior for a vesicle with $\nu = 0.7$, $Bn = 10^{-4}$, $\chi = 10$, and $\eta = 1$ is shown in Fig. 16. Note that the Reynolds number in this case is $Re = Bn\chi = 10^{-3}$. The computational domain is a box of size $[-3, 3] \times [-3, 3]$ with periodic boundary conditions in the x-directions and Dirilicht velocity boundary conditions in the y-direction. The minimum grid spacing is 6×2^{-8} with a maximum time step of 2×10^{-2}. To demonstrate the overall behavior the fluid velocity field is also included. In this situation a vortex forms at the center of the vesicle and the vesicle rotates in response. At equilibrium the fluid motion is aligned with the vesicle membrane. This indicates that particles on the membrane would travel around the vesicle.

In Ref. [44] it was shown that for Stokes flow the equilibrium inclination angle only depends on the reduced area of the vesicle and is almost independent of the applied shear rate. Here the effect of Reynolds number will be demonstrated. To see this effect consider the case of $Bn = 10^{-4}$ and $\eta = 1$ for various shear rates. The computed inclination angle is given in Fig. 17 for shear rates of $\chi = 1, 10, 100$, and 10^4 corresponding to $Re = 10^{-4}, 10^{-3}, 10^{-2}$, and 1. Fluctuations seen in the inclination angle are due to calculation of the angle and not to the underlying method. For very small values of Re the inclination angle is approximately independent of Re, consistent with the results in Ref. [44]. When the Reynolds number is raised to $Re = 1$ a significant increase in the inclination angle is observed. Investigations into this behavior are ongoing.

Our method also allows for the investigation of stiffness effects on the vesicle shape and the fluid field. Consider a vesicle with a reduced area of $\nu = 0.5$ with $\eta = 1$. For small shear rates this vesicle will reach an equilibrium angle that is independent of the applied shear rate, see above. The relative influence of the bending on the behavior of the vesicle can be captured by either fixing the shear rate and varying Bn or by fixing Bn and varying χ. Here the value $Bn = 10^{-4}$ is fixed and the equilibrium angle for shear rates of $\chi = 1$ and $\chi = 100$ are determined. The resulting equilibrium shapes and internal fluid fields are shown in Fig. 18. The inclination angle with respect to the horizontal axis for membrane 18(a) is $\theta = 0.25$ while for membrane 18(b) it is calculated to be $\theta = 0.23$. Due to the large influence of stiffness (bending) of the membrane in Fig. 18(a) the equilibrium shape is closer to the equilibrium shape observed in a stationary fluid, Fig. 18, in that the ends of the vesicle are rounded. This shape results in two internal vortices. For the case shown in Fig. 18(b) the stiffness is relatively small resulting in an elliptical vesicle as was previously observed. In this instance there is only a single internal vortex. The fluid field outside of both vesicles is not that different than the result seen in Fig. 16 and thus are not shown. Knowledge of how the interior fluid behaves would be crucial if vesicles are to be used as microreactors [6, 7].

A viscosity ratio above the critical value results in a change of behavior, from tank-treading to tumbling, with the vesicle becoming slightly more solid-like [1]. In this situation the vesicle will rotate about its center of mass. Consider a vesicle of reduced area $\nu = 0.7$ with $Bn = 10^{-4}$ and $\chi = 10$, giving $Re = 10^{-3}$. Under these conditions Keller
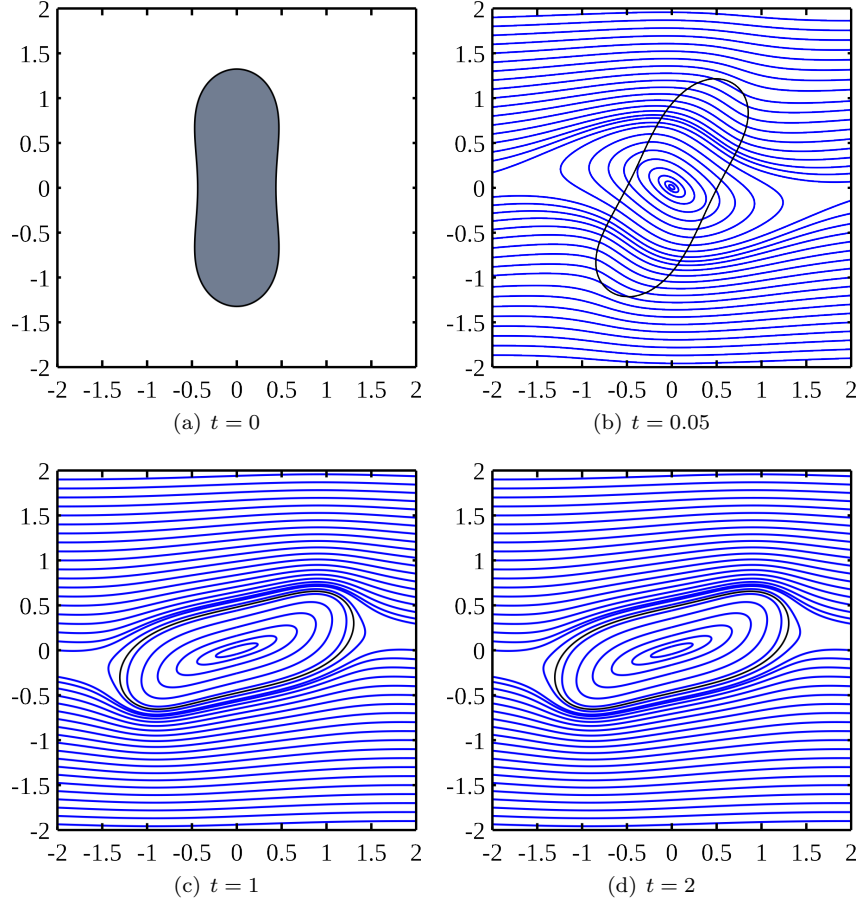
Figure 16: Behavior of a vesicle in simple shear flow with $\nu = 0.7$, $Bn = 10^{-4}$, $\chi = 10$, $Re = 10^{-3}$, and $\eta = 1$ for the normalized times indicated. Notice that a stable equilibrium configuration is achieved and a vortex forms in the interior of the vesicle and that the fluid is tangent to the membrane, indicating the tank-treading behavior.

and Skalak predict a critical viscosity ratio of 4.1 [55]. Take as an example a vesicle with a viscosity ratio of $\eta = 5$ placed in a computational domain of $[-3, 3] \times [-3, 3]$ with periodic boundary conditions in the x-direction and Dirilicht velocity boundary conditions in the y-direction. The behavior over time is shown in Fig. 19. In addition to the rotation of the vesicle a large shape change is observed. A highly curved shape is observed when the long-axis of the vesicle is aligned perpendicular to the flow field, Fig. 19(d). As the vesicle rotates the shape becomes more elliptical, Figs. 19(b) and 19(e). This change in shape is due to the relative effects of the shear flow and bending. When perpendicular to the flow the bending energy can not overcome the forces associated with the fluid flow. As the vesicle aligns itself to the flow field, the external fluid forces diminish allowing the vesicle to relax and reduce the bending energy. This type of behavior has been previously observed in numerical simulations of red blood cells in large domains [56].
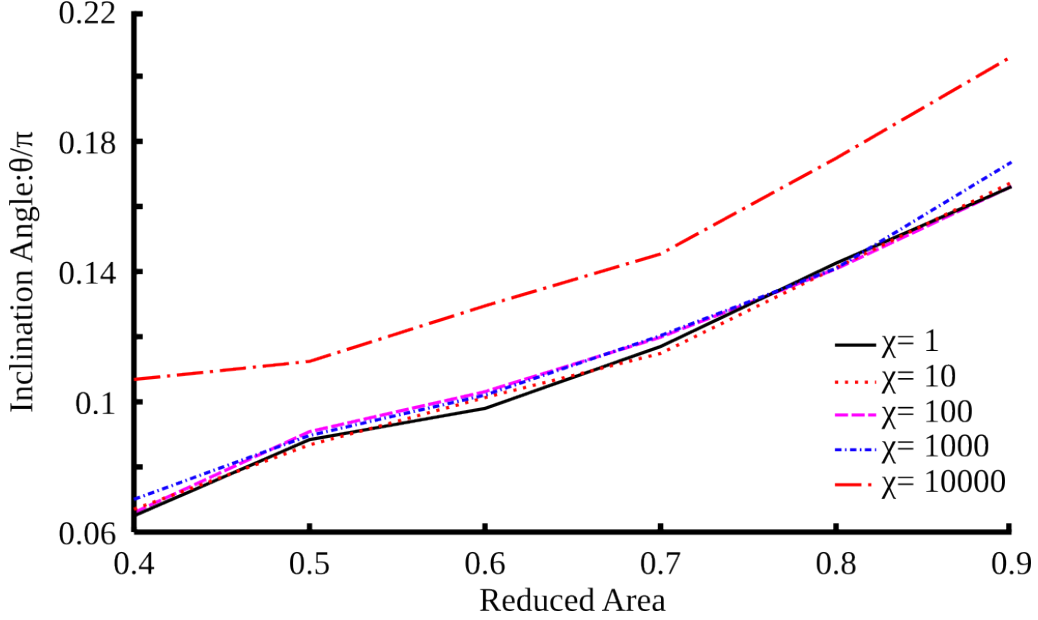
24

Figure 17: The equilibrium angle of inclination for vesicles of varying reduced areas under simple shear flow. As seen in ref. [44] The observed inclination angle is nearly independent of shear rate.

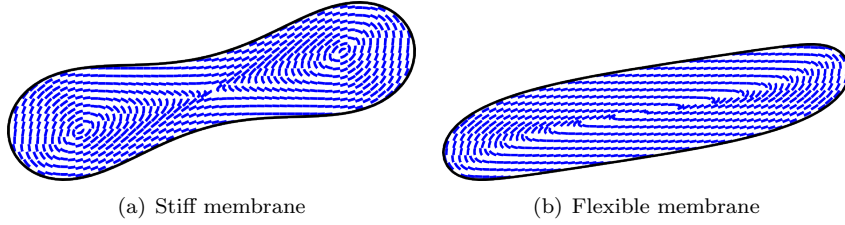(a) Stiff membrane   (b) Flexible membrane

Figure 18: The equilibrium shape and fluid field in the interior of two vesicles in simple shear flow, both with $\nu = 0.5$, $Bn = 10^{-4}$ and $\eta = 1$ for different applied shear rates. (a) $\chi = 1$ and $Re = 10^{-4}$. (b) $\chi = 100$ and $Re = 10^{-2}$. The result in (a) clearly show two vortexes while (b) has one. Both vesicles demonstrate similar equilibrium inclination angles.

The influence of the Reynolds number on the behavior of vesicles can be investigated using the method developed. In addition to the result shown in Fig. 19 vesicles with $\nu = 0.7$ and $\eta = 5$ are allowed to evolve in a simple shear of strength $\chi = 10^{-4}$ under bending numbers ranging from $Bn = 10^{-3}$ to $Bn = 1$. This results in Reynolds numbers ranging from 10^{-2} to 10. The results are shown in Fig. 20. To remove any difference in observed behavior due to the longer startup times (the amount of time before the vesicles begins to rotate) at higher Reynolds numbers the results shown here begin with an initial velocity field of $\boldsymbol{u}_0 = (\chi y, 0)$. Results show that at higher Reynolds numbers the flow transitions back to the tank-treading case. The effects of Reynolds number on

(a) $t = 0$

(b) $t = 0.5$

(c) $t = 1$

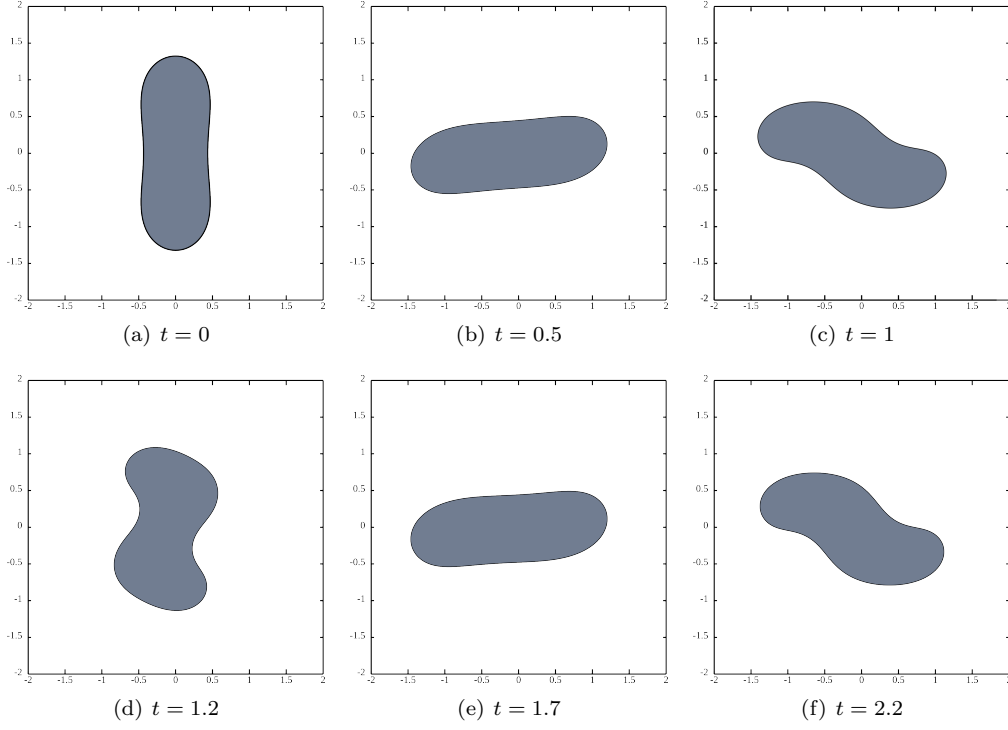(d) $t = 1.2$

(e) $t = 1.7$

(f) $t = 2.2$

Figure 19: Snapshots of the dynamic behavior of a vesicle with $\nu = 0.7$ and $\eta = 5$ under a simple shear of strength of $\chi = 10$. The bending parameter is $Bn = 10^{-4}$, resulting in $Re = 10^{-3}$. This viscosity ratio is above the classical critical viscosity ratio given by Keller and Skalak [55].

lipid vesicles is a current research topic as it is yet to determined if the result seen here is truly due to a change in Reynolds number or if it is due to change in the influence of the bending rigidity of the interface.

(a) $Bn = 10^{-3}$ $Re = 10^{-2}$

(b) $Bn = 10^{-2}$ $Re = 10^{-1}$

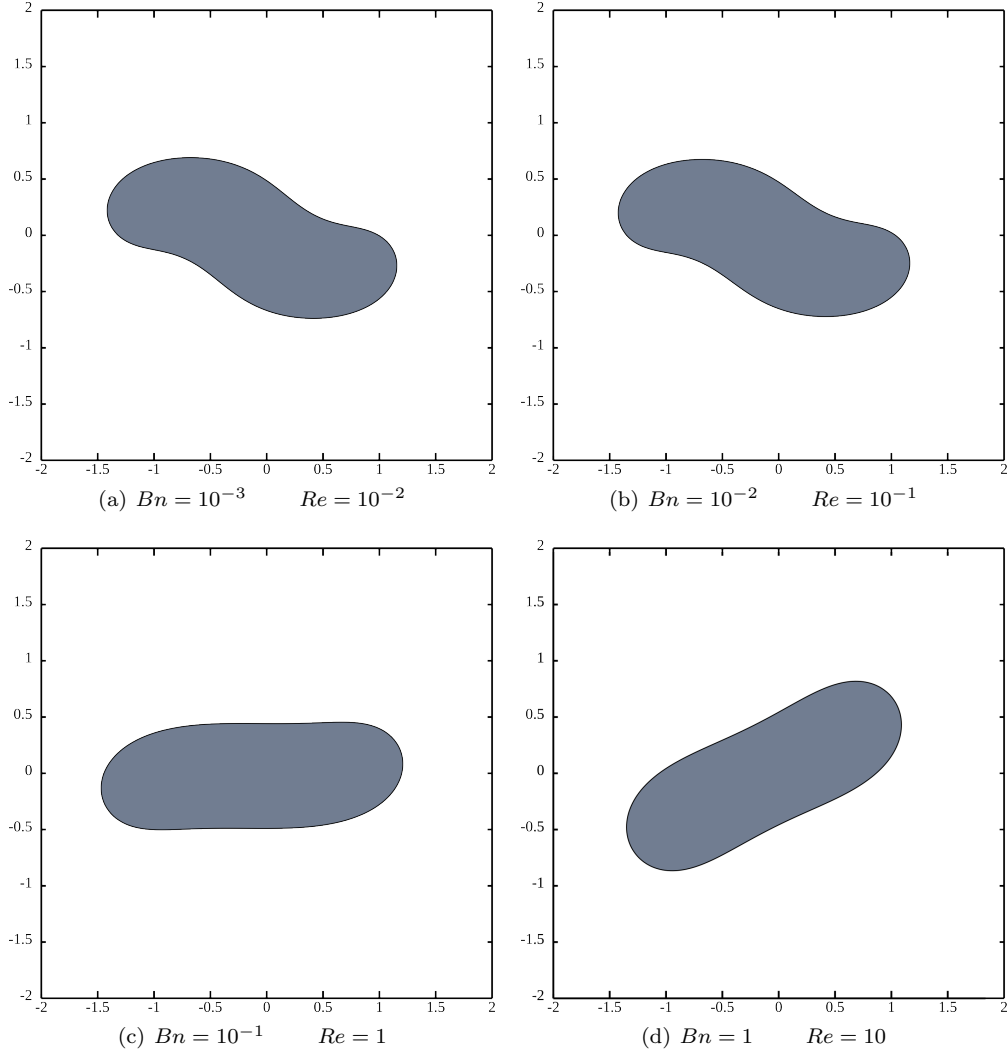(c) $Bn = 10^{-1}$ $Re = 1$

(d) $Bn = 1$ $Re = 10$

Figure 20: The instantaneous position of vesicles under simple shear at different Reynolds numbers at time $t = 1$. In all situations the shear flow strength is $\chi = 10$, resulting in a Reynolds number of $Re = 10Bn$. The results in (a)-(c) are instantaneous positions while (d) is the equilibrium configuration. Results show that a change in the Reynolds number of the system drastically changes the behavior of the vesicle.

27

5.3. Local versus Global Tension

The local, pointwise incompressibility constraint enforced in this scheme is not the only possiblity for membrane conservation. It is also possible to only enforce global membrane length conservation (but not local incompressibility) through the use of a time-dependent uniform tension, similar to the Lagrange multipliers used by Du [19]. In the global conservation scheme a uniform tension would be defined as $\gamma(t) = \gamma_0(L(t) - L_0)$, where $L(t)$ is the membrane length at the current time, L_0 is the initial membrane length, and γ_0 is a constant. To consider only global conservation the final step of the scheme, Eq. (27), is ignored and a uniform tension body term is added to Eq. (24) in the form of $-\delta(\phi)\gamma(t)\kappa\nabla\phi$.

To compare the local incompressiblity with the globally conservation scheme consider a vesicle with a reduced area of $\nu = 0.7$, a bending number of $Bn = 10^{-4}$, and a viscosity ratio of $\eta = 4.5$ placed in a computational domain of size $[-3, 3] \times [-3, 3]$ with periodic boundary conditions in the x-directions and Dirilicht velocity boundary conditions in the y-direction. A shear flow of strength $\chi = 1$ is then applied to the vesicle. The global conservation (uniform tension) scheme is implemented using a parameter of $\gamma_0 = 10^7$. Other than the form of the tension all other computational parameters including grid spacing and time step are equal. The result for various times is shown in Fig. 21. With these parameters the classical lipid vesicle theory predicts that the vesicle should undergo tumbling. As the figures show the vesicle with local incompressibility does undergo tumbling while that with a global conservation does not. This demonstrates that it is not enough to only enforce global membrane length conservation when investigating lipid vesicles, local incompressibility should also be enforced. It should be noted that our computations do show that a vesicle constrained only by global membrane length conservation will have tumbling solutions. This tank treading - tumbling transition will occur at a higher viscosity ratio than the one predicted by enforcing local incompressibility.
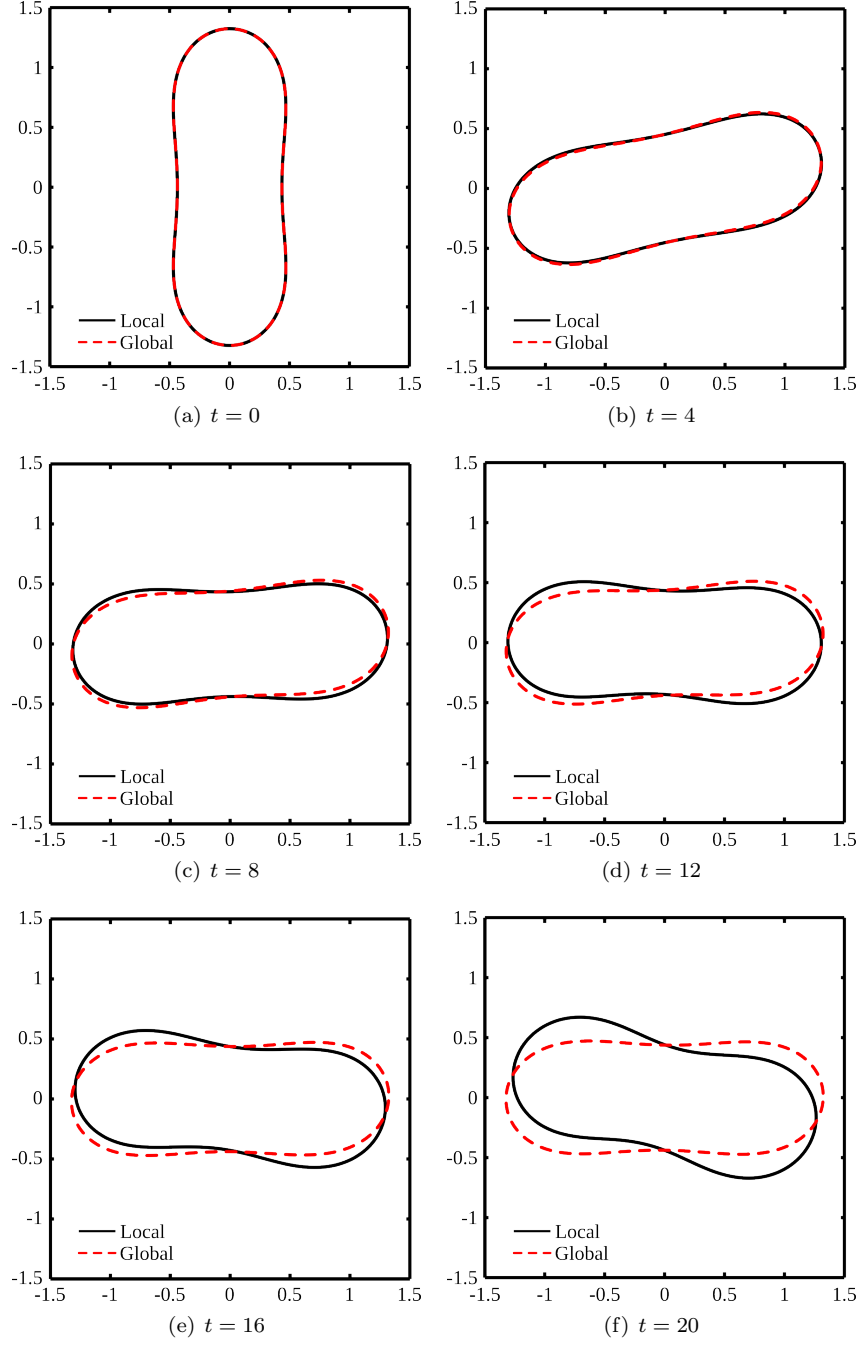
Figure 21: A comparison of a single vesicle under simple shear using two different membrane length conservation schemes. The first is the local, pointwise conservation scheme presented here. The other is a global tension given by $\gamma(t) = 10^7 \times (L(t) - L_0)$, where $L(t)$ is the membrane length at the current time and L_0 is the initial membrane length. The behavior using the two different conservation schemes is different.

6. Results: Multiple Vesicles

Results involving multiple vesicles are now presented. The methods outlined above handle multiple vesicles naturally.

6.1. Tumbling of Two Vesicles

First consider two isolated vesicles with a reduced area of $\nu = 0.5$ and viscosity ratio of $\eta = 5$ in a shear flow of strength $\chi = 100$ with $Bn = 10^{-4}$, giving $Re = 10^{-2}$. These results are computed in the domain given by $[-5, 5] \times [-5, 5]$ with periodic boundary conditions in the x-direction and Dirilicht boundary conditions in the y-direction. The short-time results are shown in Fig. 22. Initially the two vesicles rotate as if they were isolated. Due to the interaction between the two vesicles they begin to rotate about each other before being captured by the external flow. This initial behavior is similar to the Stokes flow result presented in Ref. [25].
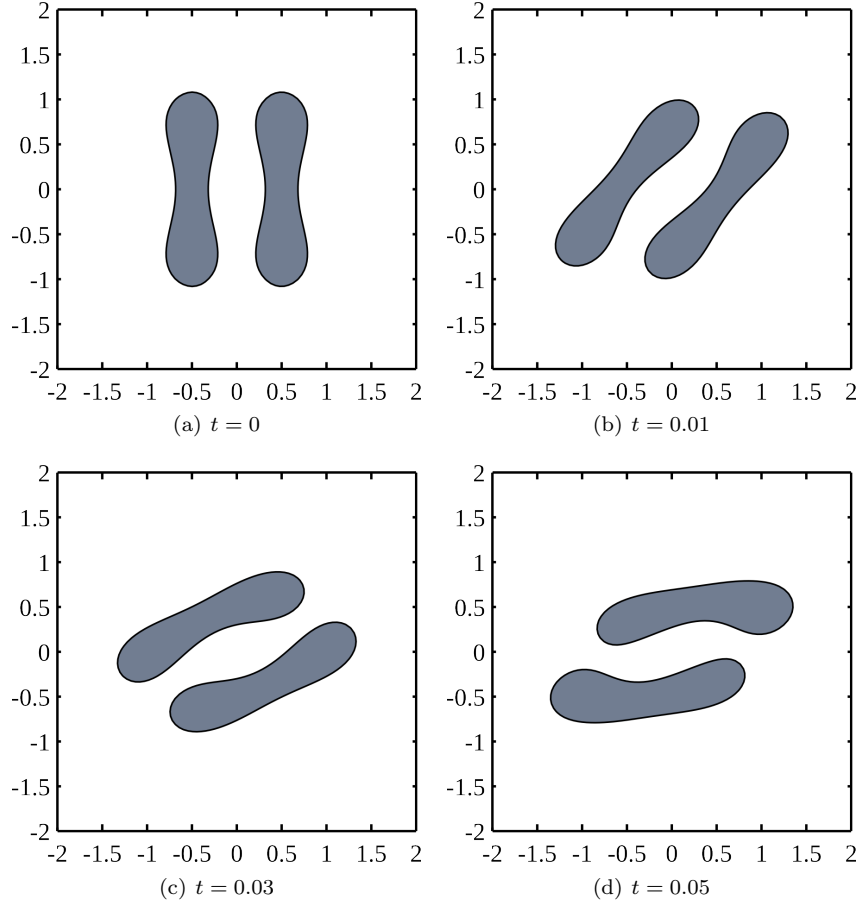

Figure 22: Snapshots of the position of two vesicles under the influence of a shear flow of strength $\chi = 100$ with $Bn = 10^{-4}$ and $\eta = 5$. The Reynolds number is $Re = 10^{-2}$.

30

The long-term results are shown in Fig. 23. The behavior of the vesicles is seen to be a combination of rotation due to the shear flow and flattening of the vesicle due to the high bending energy of the resulting configurations. The interactions of the vesicles also induces further rotation of the vesicles.
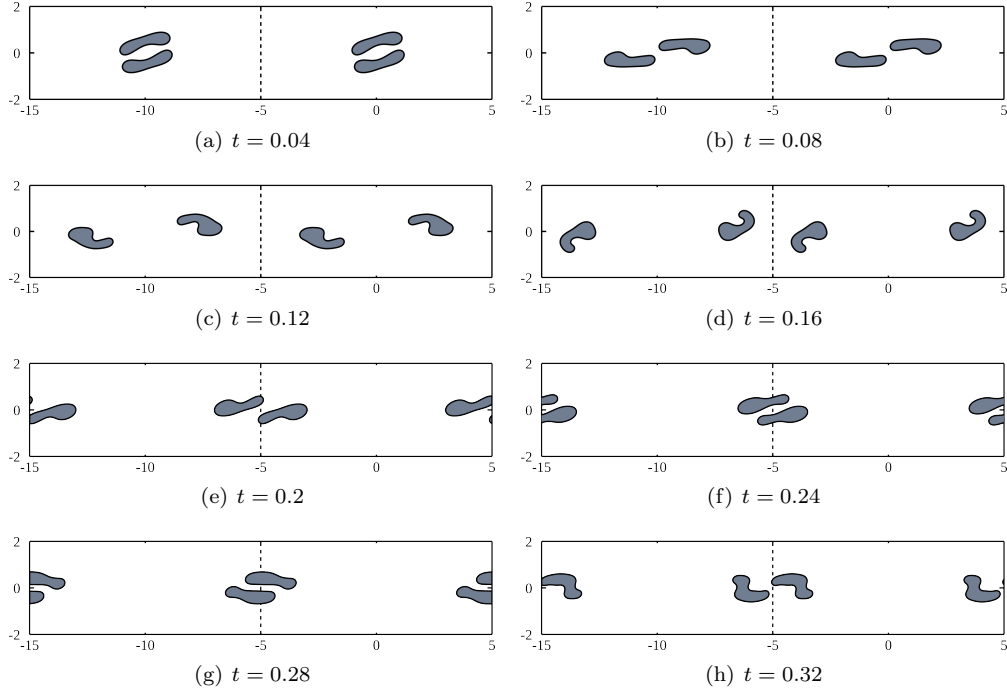

Figure 23: Snapshots of the position of two vesicles under the influence of a shear flow of strength $\chi = 100$, with $Bn = 10^{-4}$ and $\eta = 5$, resulting in $Re = 10^{-2}$. Two computational domains are shown side-by-side. The figures only show the region given by $|y| \leq 2$.

6.2. Many Vesicles in Shear Flow

Next consider a large number of vesicles under the influence of shear flow. Specifically, consider 30 vesicles of reduced area $\nu = 0.5$ arranged in a regular array contained in a $[-5, 5] \times [-5, 5]$ computational domain with periodic boundary conditions in the x-direction and wall boundary conditions in the y-direction, Fig. 24. Apply a shear flow with strength $\chi = 100$ and assume parameters of $Bn = 10^{-2}$ and $\eta = 10$. The Reynolds number here is $Re = 1$. Due to the highly packed nature of the system the vesicles are not able to rotate as seen in Figs. 22 and 23. Instead the vesicles reach an equilibrium angle and undergo linear motion. The upper and lower rows have normalized speeds of 150 to the right and left, respectively. The center row does not migrate, only undergoing a slight rotation.

Next, consider 10 vesicles with $\nu = 0.5$ and $\eta = 5$ randomly placed in a computational domain of $[-2, 2] \times [-2, 2]$ subject to a shear flow of strength $\chi = 10^4$. Given $Bn = 10^{-4}$ this gives a Reynolds number of $Re = 1$. Periodic boundary conditions are applied in the

31

(a) $t = 0$ (b) $t = 0.005$
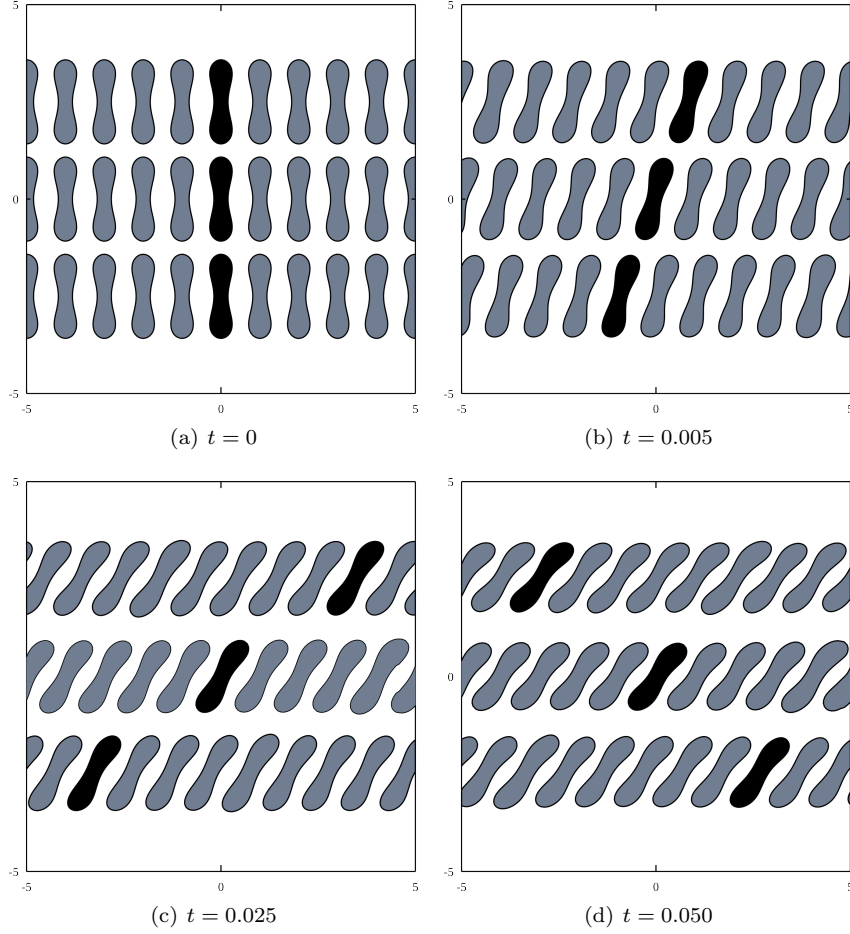
(c) $t = 0.025$ (d) $t = 0.050$

Figure 24: Snapshots of the position of many close-packed vesicles under the influence of a shear flow of strength $\chi = 100$, with $Bn = 10^{-2}$ ($Re = 1$), and $\eta = 10$. Individual vesicles have been marked to make tracking easier. After an initial startup the vesicles reach a steady velocity, with both the upper and lower row of vesicles moving at a normalized speed of 150. After reaching the shown angle the center row is stationary.

x-direction while Dirilicht velocity conditions are applied in the y-direction. The result up to a time of $t = 8 \times 10^{-4}$ is given in Fig. 25. Unlike the close-packed case (Fig. 24), the additional area surrounding the vesicles allows for a number of different behaviors, including linear translation (upper and lower marked vesicles) and circulation (center marked vesicle). Note that in general the vesicles align with the flow field, similar to the tank-treading case of a single vesicle under simple shear.

6.3. Pressure Driven Flow

A result due to pressure-driven Poiseuille flow is also presented. Four vesicles with $\nu = 0.5$ are placed into a domain given by $[-2, 2] \times [-2, 2]$ with periodic boundary
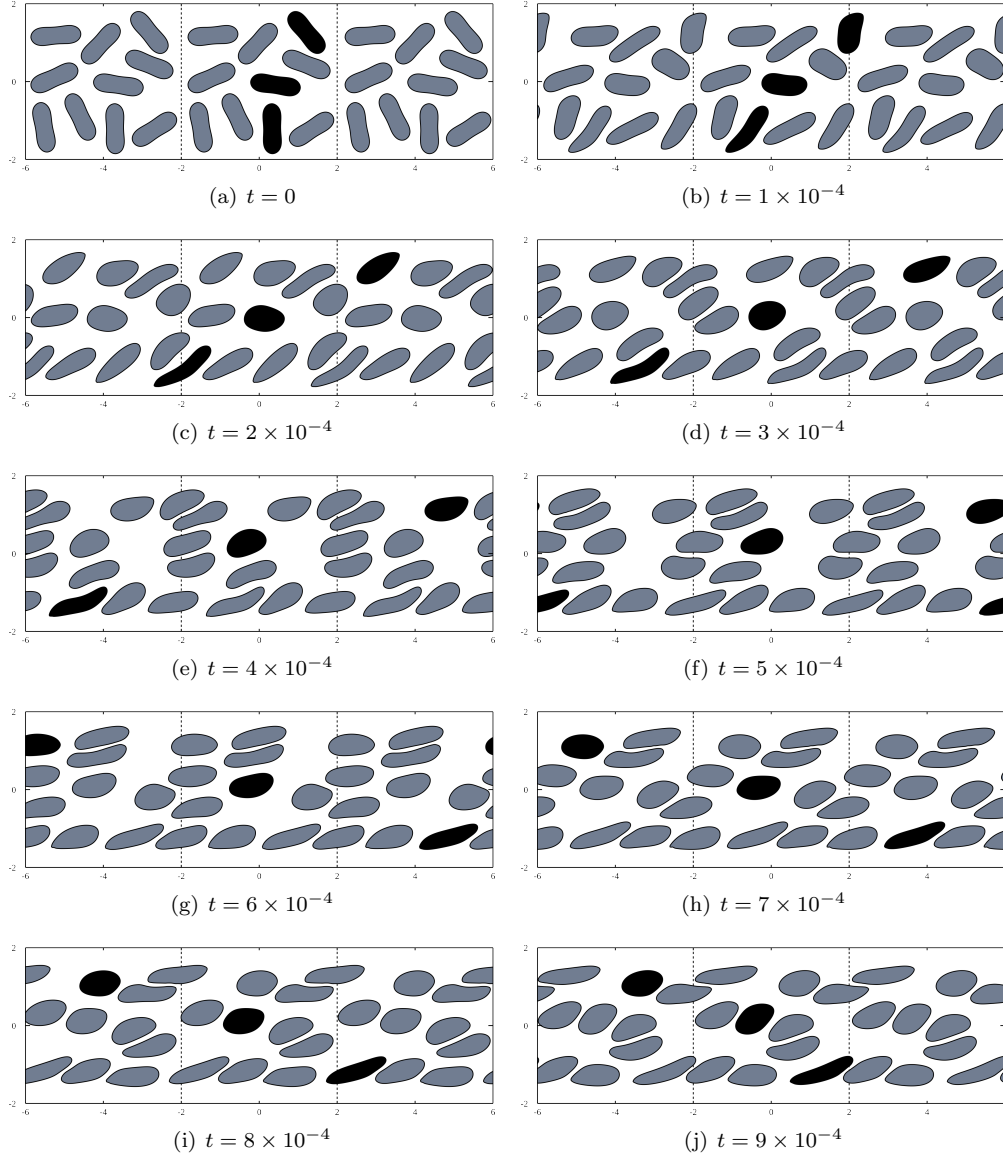
Figure 25: Snapshots of the position of many randomly placed vesicles under the influence of a shear flow of strength $\chi = 10^4$, with $Bn = 10^{-4}$ $(Re = 1)$, and $\eta = 5$. Several individual vesicles have been marked to make tracking easier. A wide variety of behavior is observed, including linear translation and vesicle circulation.

conditions in the x-direction and no-slip boundary conditions in the y-direction. Each vesicle is placed slightly off the center line. It is expected that the close-packed nature of the system will influence the result. A pressure gradient of magnitude $\Delta p = -5000$ is applied in the x-direction. The relationship between the maximum velocity in a vesicle-

free domain and the pressure gradient is given by $u_{max} = -Bn \times \Delta P \times H^2/8$, where H is the total domain height. Assuming $Bn = 10^{-2}$ this gives $u_{max} = 100$. The viscosity ratio is taken to be $\eta = 5$. The position of the vesicles over time can be seen in Fig. 26.

The behavior observed in Fig. 26 is similar to what has been experimentally observed for highly packed cells traveling in a capillary tube of comparable size to the cell diameter [57]. The cells arrange themselves into a single file, positioned slightly off the centerline. The equilibrium shape of the cells has been described as slipper-like, with a thinner and elongated portion of the cell away from the centerline and a slight bulge near the front edge.

6.4. Vesicle Merging

As a final demonstration of the method the merging of two vesicles is presented. Here two vesicles placed a small distance apart are considered. An attractive force is added to the Navier-Stokes equations, specifically Eq. (24), in the form of $\boldsymbol{F}_a = H\boldsymbol{r}/\|\boldsymbol{r}\|^3$, where H is a constant. The vector r represents the closest distance between interface points on the seperate bodies. Let $\boldsymbol{x}$ be a grid point and $\boldsymbol{cp}_A(\boldsymbol{x})$ be the closest point to $\boldsymbol{x}$ on body A. The vector r is equal to the spatial vector from $\boldsymbol{cp}_A(\boldsymbol{x})$ to the closest point to $\boldsymbol{cp}_A(\boldsymbol{x})$ on the other body, B. The overall force scales as the seperation distance between the two bodies squared, similar to the attractive van der Waals force between macroscopic spherical bodies. Please note that while the force is similar to realistic forces, it was not chosen to model any particular physical process, but simply as a means to induce merging.

The merging of two vesicles with an initial reduced area of $\nu = 0.96$ and a viscosity ratio of $\eta = 5$ with $Bn = 0.02$ is shown in Fig. 27. The attraction parameter is taken to be $H = 2 \times 10^4$. The vesicles are placed in a computational domain of size $[-3, 3] \times [-3, 3]$ with zero velocity boundary conditions. The initial shape of the vesicles was chosen to ensure that the point of initial contact would occur at the center of the domain. After merging the vesicle begins to relax due to the bending energy. The new reduced area is $\nu = 0.48$ and thus the vesicle will attempt to reach a biconcave shape.

7. Conclusion and Future Work

Here a new level-set based model for the motion of lipid vesicles in general flows has been presented. The level set method allows for general situations to be investigated, including single and multiple-vesicle systems. To address the multiple constraints on the fluid system a novel four-step projection method to solve for the fluid field has been developed. The additional projection step is required to enforce the surface-incompressibility of the vesicle membrane, and can easily be added to existing code bases.

Convergence studies verify the projection operator and the overall scheme. While only presented as first-order in time and second-order in space, higher order schemes are possible. The dynamic behavior of a lipid vesicles under various flow conditions have also been presented.

Improvements to the scheme presented here include improving the time-integration scheme. Future work utilizing this scheme will include the addition of external field effect such as electrostatic interactions. The constraint that the boundaries of the domain remain flat will also be relaxed. This is needed to model more physiologically interesting
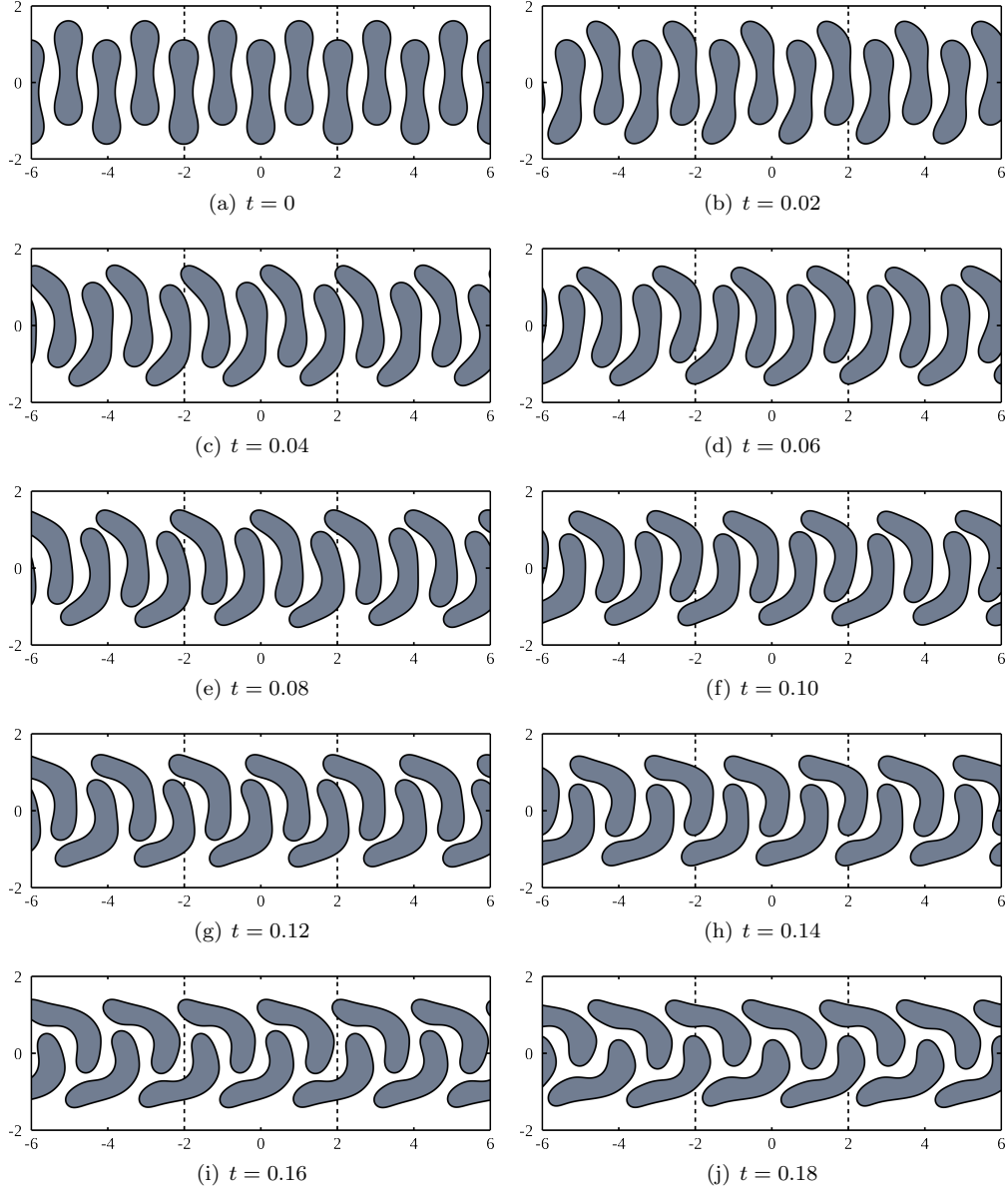
Figure 26: Snapshots of the position of multiple vesicles under pressure induced Poiseuille flow with an applied pressure gradient of $\Delta p = -5000$, $Bn = 0.01$, and $\eta = 1$. Due to the initial vesicle positions being off the center line non-symmetric shapes are observed.

situations. Finally, it is planned to extend this work to three dimensions. The mechanics of the membrane become more complicated and can be modelled using the complete Helfrich surface energy of a vesicle [33]. Once the new surface energy is taken into
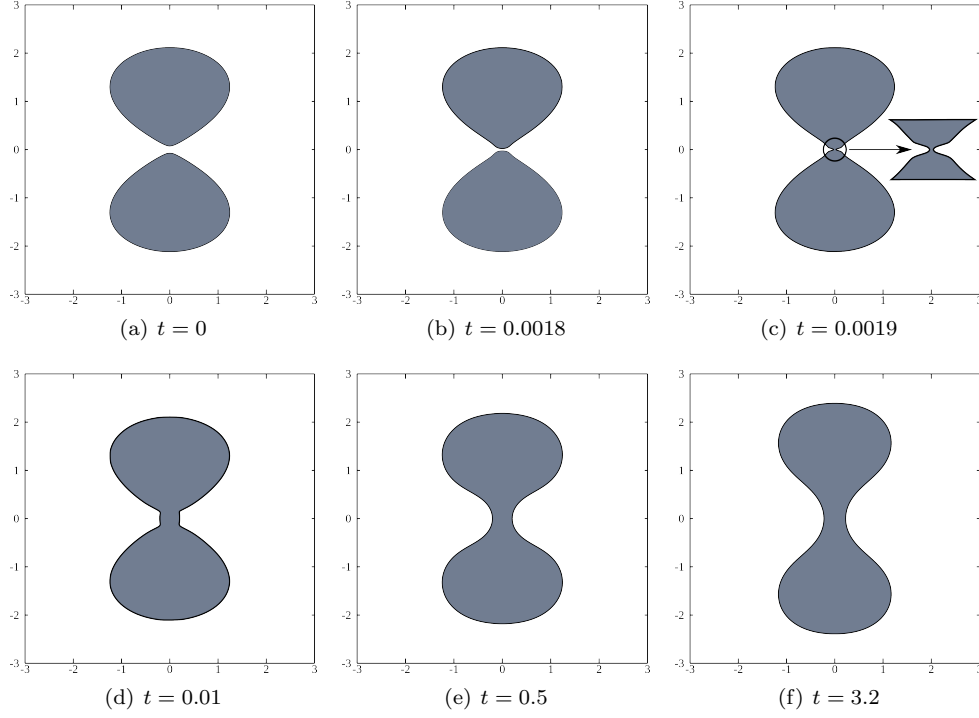
35

Figure 27: Snapshots of the merging of two vesicles under the influence of an attractive force scaling as $1/d^2$ where d is the distance between the two vesicles. The bending number was set to $Bn = 0.02$ while a viscosity ratio of $\eta = 5$ was used.

account the extension to three dimensions becomes straightforward. [33]

References

[1] M. Abkarian, A. Viallat, Vesicles and red blood cells in shear flow, Soft Matter 4 (4) (2008) 653–657.

[2] U. Seifert, Configurations of fluid membranes and vesicles, Advances In Physics 46 (1) (1997) 13–137.

[3] V. Kantsler, V. Steinberg, Transition to tumbling and two regimes of tumbling motion of a vesicle in shear flow, Physical Review Letters 96 (3) (2006) 036001.

[4] V. Kantsler, E. Segre, V. Steinberg, Dynamics of interacting vesicles and rheology of vesicle suspension in shear flow, EPL 82 (5) (2008) 58005.

[5] T. Allen, P. Cullis, Drug delivery systems: Entering the mainstream, Science 303 (5665) (2004) 1818–1822.

[6] A. Fischer, A. Franco, T. Oberholzer, Giant vesicles as microreactors for enzymatic mrna synthesis, Chembiochem 3 (5) (2002) 409–417.

[7] V. Noireaux, A. Libchaber, A vesicle bioreactor as a step toward an artificial cell assembly, Proceedings of The National Academy of Sciences of The United States of America 101 (51) (2004) 17669–17674.

[8] G. Coupier, B. Kaoui, T. Podgorski, C. Misbah, Noninertial lateral migration of vesicles in bounded poiseuille flow, Physics of Fluids 20 (11) (2008) 111702.

[9] B. Kaoui, G. Coupier, C. Misbah, T. Podgorski, Lateral migration of vesicles in microchannels: effects of walls and shear gradient, Houille Blanche-revue Internationale De L Eau (5) (2009) 112–119.

[10] H. L. Goldsmith, Red cell motions and wall interactions in tube flow., Federation proceedings 30 (5) (1971) 1578–1590.

[11] M. Abkarian, A. Viallat, Dynamics of vesicles in a wall-bounded shear flow, Biophysical Journal 89 (2) (2005) 1055–1066.

[12] P. Vlahovska, R. Gracia, Dynamics of a viscous vesicle in linear flows, Physical Review E 75 (1) (2007) 016313.

[13] P. Olla, The behavior of closed inextensible membranes in linear and quadratic shear flows, Physica A 278 (1-2) (2000) 87–106.

[14] J. T. Schwalbe, P. M. Vlahovska, M. J. Miksis, Monolayer slip effects on the dynamics of a lipid bilayer vesicle in a viscous flow, Journal of Fluid Mechanics 647 (2010) 403–419.

[15] V. Lebedev, K. Turitsyn, S. Vergeles, Nearly spherical vesicles in an external flow, New Journal of Physics 10 (2008) 043044.

[16] F. Campelo, A. Hernandez-Machado, Dynamic model and stationary shapes of fluid vesicles, European Physical Journal E 20 (1) (2006) 37–45.

[17] F. Feng, W. Klug, Finite element modeling of lipid bilayer membranes, Journal of Computational Physics 220 (1) (2006) 394–408.

[18] T. Biben, C. Misbah, Tumbling of vesicles under shear flow within an advected-field approach, Physical Review E 67 (3) (2003) 031908.

[19] Q. Du, C. Liu, X. Wang, Simulating the deformation of vesicle membranes under elastic bending energy in three dimensions, Journal of Computational Physics 212 (2) (2006) 757–777.

[20] Q. Du, C. Liu, R. Ryham, X. Wang, Energetic variational approaches in modeling vesicle and fluid interactions, Physica D: Nonlinear Phenomena 238 (2009) 923–930.

[21] Q. Du, J. Zhang, Adaptive finite element method for a phase field bending elasticity model of vesicle membrane deformations, SIAM Journal on Scientific Computing 30 (3) (2008) 1634–1657.

[22] G. Ghigliotti, T. Biben, C. Misbah, Rheology of a dilute two-dimensional suspension of vesicles, Journal of Fluid Mechanics 653 (2010) 489–518.

[23] D. Jamet, C. Misbah, Towards a thermodynamically consistent picture of the phase-field model of vesicles: local membrane incompressibility, Phys. Rev. E 76 (2007) 051907.

[24] S. Veerapaneni, D. Gueyffier, G. Biros, D. Zorin, A numerical method for simulating the dynamics of 3d axisymmetric vesicles suspended in viscous flows, Journal of Computational Physics 228 (19) (2009) 7233–7249.

[25] S. Veerapaneni, D. Gueyffier, D. Zorin, G. Biros, A boundary integral method for simulating the dynamics of inextensible vesicles suspended in a viscous fluid in 2d, Journal of Computational Physics 228 (7) (2009) 2334–2353.

[26] J. B. Freund, Leukocyte margination in a model microvessel, Physics of Fluids 19 (2) (2007) 023301.

[27] C. Pozrikidis, Modeling and simulation of capsules and biological cells, CRC Press, 2003, Ch. Shell theory for capsules and shells., pp. 35–102.

[28] S. Kessler, R. Finken, U. Seifert, Swinging and tumbling of elastic capsules in shear flow, Journal of Fluid Mechanics 605 (2008) 207–226.

[29] P. Butti, M. Intaglietta, H. Reimann, C. Holliger, A. Bollinger, M. Anliker, Capillary red blood-cell velocity-measurements in human nailfold by videodensitometric method, Microvascular Research 10 (2) (1975) 220–227.

[30] P. Vennemann, R. Lindken, J. Westerweel, In vivo whole-field blood velocity measurement techniques, Experiments in Fluids 42 (2007) 495–511.

[31] H. Hinghofer-Szalkay, J. E. Greenleaf, Continuous monitoring of blood volume changes in humans, Journal of Applied Physiology 63 (3) (1987) 1003–1007.

[32] D. Marsh, Elastic curvature constants of lipid monolayers and bilayers, Chemistry And Physics of Lipids 144 (2) (2006) 146–159.

[33] W. Helfrich, Elastic properties of lipid bilayers - theory and possible experiments, Zeitschrift Fur Naturforschung C - A Journal of Biosciences C 28 (11-1) (1973) 693–703.

[34] U. Seifert, Fluid membranes in hydrodynamic flow fields: Formalism and an application to fluctuating quasispherical vesicles in shear flow, The European Physical Journal B 8 (3) (1999) 405–415.

[35] J. Nave, R. Rosales, B. Seibold, A gradient-augmented level set method with an optimally local, coherent advection scheme, Journal of Computational Physics 229 (10) (2010) 3802–3827.

[36] C. B. Macdonald, S. J. Ruuth, The implicit closest point method for the numerical solution of partial differential equations on surfaces, SIAM Journal on Scientific Computing 31 (6) (2010) 4330.

[37] J. Sethian, Fast marching methods, Siam Review 41 (2) (1999) 199–235.

[38] C. Min, F. Gibou, A second order accurate projection method for the incompressible navier-stokes equations on non-graded adaptive grids, Journal of Computational Physics 219 (2) (2006) 912–929.

[39] J. Sethian, P. Smereka, Level set methods for fluid interfaces, Annual Review of Fluid Mechanics 35 (2003) 341–372.

[40] S. Osher, R. Fedkiw, Level set methods: An overview and some recent results, Journal of Computational Physics 169 (2) (2001) 463–502.

[41] D. Salac, W. Lu, Stability and shape evolution of voids and channels due to surface misfit, International Journal of Solids And Structures 45 (13) (2008) 3793–3806.

[42] P. Smereka, Semi-implicit level set methods for curvature and surface diffusion motion, Journal of Scientific Computing 19 (1-3) (2003) 439–456.

[43] Y. Chang, T. Hou, B. Merriman, S. Osher, A level set formulation of eulerian interface capturing methods for incompressible fluid flows, Journal of Computational Physics 124 (2) (1996) 449–464.

[44] M. Kraus, W. Wintz, U. Seifert, R. Lipowsky, Fluid vesicles in shear flow, Physical Review Letters 77 (17) (1996) 3685–3688.

[45] D. Salac, Augmented fast marching method for level set reinitalization, In Preparation.

[46] D. Chopp, Some improvements of the fast marching method, Siam Journal On Scientific Computing 23 (1) (2001) 230–244.

[47] D. Chopp, Another look at velocity extensions in the level set method, Siam Journal of Scientific Computing In Review.

[48] J. Sethian, A fast marching level set method for monotonically advancing fronts, Proceedings of The National Academy of Sciences of The United States of America 93 (4) (1996) 1591–1595.

[49] D. Brown, R. Cortez, M. Minion, Accurate projection methods for the incompressible navier-stokes equations, Journal of Computational Physics 168 (2) (2001) 464–499.

[50] M. Sussman, A. Almgren, J. Bell, P. Colella, L. Howell, M. Welcome, An adaptive level set approach for incompressible two-phase flows, Journal of Computational Physics 148 (1) (1999) 81–124.

[51] D. Xiu, G. Karniadakis, A semi-lagrangian high-order method for navier-stokes equations, Journal of Computational Physics 172 (2) (2001) 658–684.

[52] C. B. Macdonald, S. J. Ruuth, Level set equations on surfaces via the closest point method, Journal of Scientific Computing 35 (2) (2008) 219–240.

[53] S. Ruuth, B. Merriman, A simple embedding method for solving partial differential equations on surfaces, Journal of Computational Physics 227 (3) (2008) 1943–1961.

[54] J. Deschamps, V. Kantsler, E. Segre, V. Steinberg, Dynamics of a vesicle in general flow, Proceedings of The National Academy of Sciences of The United States of America 106 (28) (2009) 11444–11447.

[55] S. Keller, R. Skalak, Motion of a tank-treading ellipsoidal particle in a shear-flow, Journal of Fluid Mechanics 120 (1982) 27–47.

[56] P. Bagchi, Mesoscale simulation of blood flow in small vessels, Biophysical Journal 92 (6) (2007) 1858–1877.

[57] C. Pozrikidis, Axisymmetric motion of a file of red blood cells through capillaries, Physics of Fluids 17 (3) (2005) 031503.